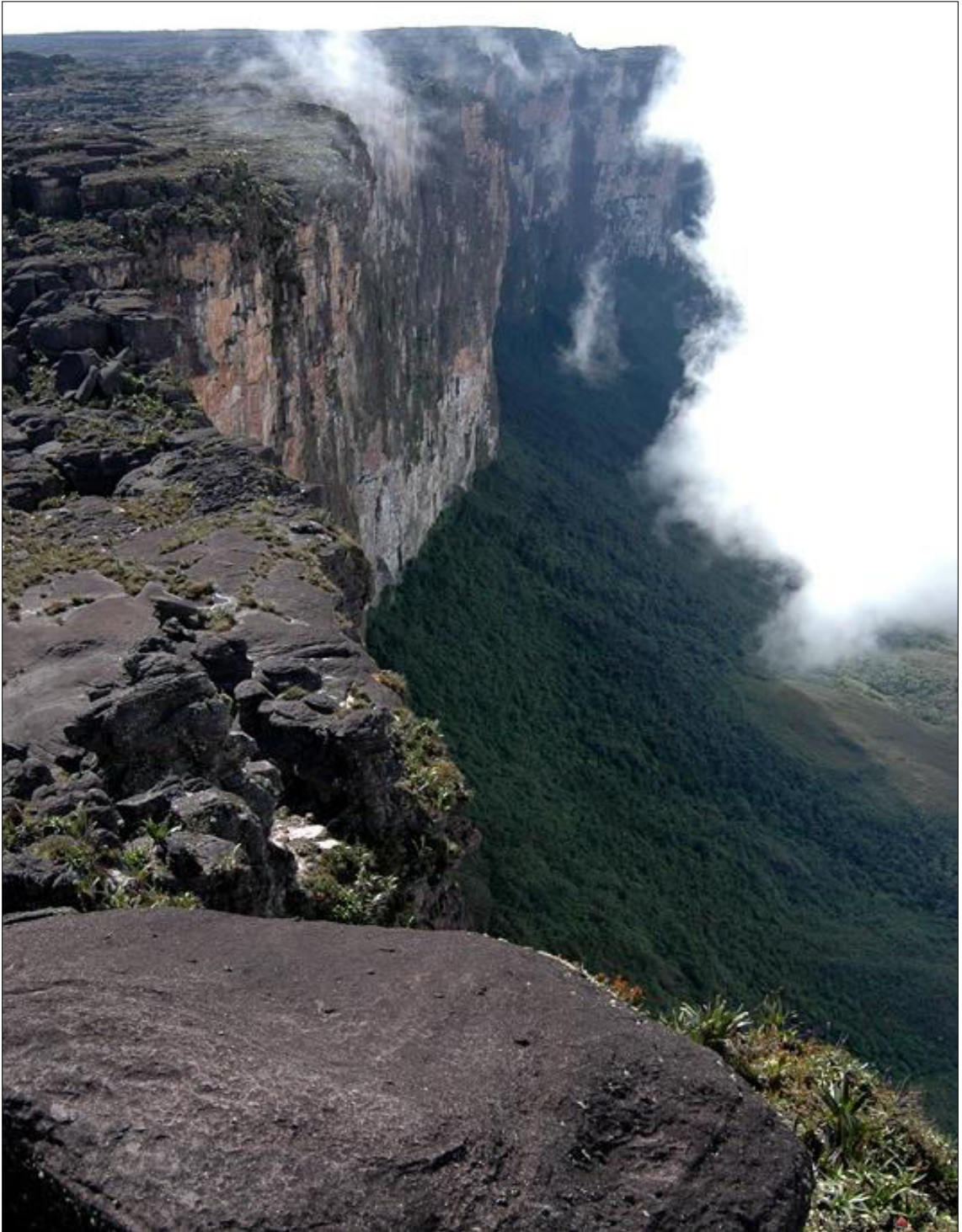


Vertical Displacement in the Pachmarhi

Dr. N.L. Dongre



ABSTRACT - To understand the Pachmarhi geological stage and its structure, an analytical method is derived, which gives the elastic response of a homogeneous rock layer to two-dimensional distributions of vertical displacement applied along its lower boundary. Displacement field, stress distribution, and distortional strain-energy density diagrams are presented for three types of displacement applied at the lower boundary of 5 kilometer thick layers possessing average sedimentary rock properties. These three types of displacements are: (1) sinusoidal vertical displacement and no horizontal displacement; (2) an approximate step in vertical displacement and no horizontal displacement; and (3) sinusoidal vertical and horizontal displacement (horizontal displacement 90° out of phase with the vertical). Displacement fields and stress distributions for each type of applied displacement are nearly independent of the elastic characteristics of the layers. The magnitudes of displacement necessary to initiate fracture at some point in the layer are small (3.7 – 8.2 m) for the three types of applied displacement. For applied displacement (1) and (3), the initial fracture is a vertical tensile crack at the crest of the fold. For applied displacement (2), the initial fracture is either a vertical crack at the upper surface or a shear fracture at the lower surface. Displacement fields and fracture patterns for scale-model experiments of two problems similar to the analytical examples are presented. For a sinusoidal vertical displacement, the fracture pattern is a complex zone of normal faults which taper inward toward the axis of the fold and die out at depth. For a step in vertical displacement, the fracture pattern is (1) a series of reverse faults which start vertically at the base of the layer, curve, and intersect the upper surface at low angles, and (2) a series of normal faults dipping toward the convex side of the reverse faults. Of particular interest are the reverse faults which show that vertical movement at depth can generate low-angle faulting at the surface. Displacement fields found in the elastic analyses are good first-order approximations of displacement fields in the scale-model experiments. Points of initial fracture observed in the model experiments agree closely with those computed in the elastic analyses. The line of fracture for the curved reverse faults in the model experiments can be predicted on the basis of the Mohr fracture criterion and the stress distribution from an elastic analysis.

Introduction

Much of the Pachmarhi structural deformation is results from differential vertical movements of underlying basement rock. This paper describes an analytical and experimental investigation of the Pachmarhi, resulting from simple distributions of vertical displacement along the base of homogeneous rock layers. A special form of the general theory of elasticity is used in the analytical work, and scale models with homogeneous layers of dry sands and clay is used in the experimental work.

A purpose of the investigation is to determine:

1. The characteristics of the folding and faulting produced by simple two-dimensional distributions of applied vertical displacement along the bases of homogeneous layers.

2. The degree of similarity between a two- dimensional elastic analysis and a two- dimensional scale-model experiment of the same physical situation.

The physical situations investigated are simple idealized representations of the geologic conditions in sedimentary basins. However, investigation of these simple situations is a necessary first step toward an understanding of the more complex problems occurring in nature.

Analytical study of structure

Method

In the analytical method employed in the tectonic structural study of the Pachmathi and distributions of vertical displacement are specified along the base of a homogeneous elastic layer. The method is similar to one used by Hafner (1951) to describe the response of a homogeneous elastic layer to applied stresses. The two methods give similar results when applied to the Mahadeva geologic situations such as folding of a layer. However, for certain structures, one method may be superior.

Block faulting of sedimentary layers above a rigid basement can be represented best by specifying displacements (Hunt and Fitchener, 2001). In the Pachmarhi type of structure, adjacent blocks of basement rock are moved uniformly up or down with respect to each other. The overlying layer is undeformed by the movement in the region, where the two blocks meet.(McClay K.R.1990) The magnitude and, distribution of stress along the base 'of the layer cannot be determined in the zone of deformation. The best analytical representation can be made by using the only available information-the displacements.

An analytical method based on displacements along the base of an elastic layer has an additional advantage. Displacement can be easily measured in scale-model experiments. Therefore a comparison between model experiments and elastic analyses is possible when displacements similar to those used in the experiments are specified in the elastic analyses.

Derivation of analytical method

The analytical method is based on the theory of elasticity (Timoshenko and Goodier, 1951; Love.1944 ; Muskhelishvili,1953). Several assumptions made in this theory restrict its application to idealized representations of geologic structures. The displacements and strains must be small. The material undergoing deformation must be perfectly elastic (able to recover its initial form after removal of stresses), linearly elastic possessing a linear relationship between stress and strain), homogeneous (possessing the same specific properties through out its volume), and isotropic possessing elastic properties which are the same in all directions).

Even' with these assumptions, application of the theory of elasticity to three-dimensional geologic problems remains difficult (Murdock, J.K.,1997). However, a simplification is possible within the framework of the theory. If the lower boundary of a layer undergoes (Murrell, S.A.F. 1977) . Displacements in the x – and y – directions only, and these displacements are identical for all xy –cross sections along the z – axis from minus to plus infinity, then all xy -cross sections are in the same condition (Figure 1). Therefore, a two-dimensional analysis of a single cross section will describe the stresses and displacements along the length of the z – axis. With this procedure, two-dimensional situations similar to cross sections near the center of elongated geologic structures can be analyzed.

The nomenclature used is as follows (notation is the same as that of Timoshenko and Goodier (1951))

$\sigma_x, \sigma_y, \sigma_z$	Normal components of stress parallel to the $x -$, $y -$ and $z -$ axis
τ_{xy}	Shearing-stress component
$\sigma_1, \sigma_2, \sigma_3$	Maximum, intermediate, and minimum principal stresses
u, v	Components of displacement in the $x -$ and $y -$ directions
$\epsilon_x = \frac{\partial u}{\partial x}, \epsilon_y = \frac{\partial v}{\partial y}$	Unit elongations in the $x -$ and $y -$ directions (strains)
$\gamma_{xy} = \frac{\partial u}{\partial y} + \frac{\partial v}{\partial x}$	Shearing strain
G	Modulus of rigidity
ν	Poisson's ratio
λ	Lame's constant
$K_1 = \frac{\lambda+2G}{G} = \frac{2(1-\nu)}{1-2\nu}$	Constant used in this paper
$K_3 = 1 - K_1 = -\frac{1}{1-2\nu}$	Constant used in this paper
ρ	Density
g	Gravitational acceleration
$\nabla^2 = \frac{\partial^2}{\partial x^2} + \frac{\partial^2}{\partial y^2}$	Laplacian operator
$\alpha = m\pi/L$	Coefficient
E_d	Distortional strain-energy density
H	Thickness of the elastic layer
L	Distance between points of zero vertical displacement
B_c	Critical displacement the maximum amount of displacement without failure
σ	Normal stress across a potential fracture plane
τ	Shearing stress along a potential fracture plane
τ_0	Shear stress necessary to overcome the initial shear strength due cohesion

\emptyset Angle of internal friction θ **Angle between line of fracture and principal stress**

The sign convention used for normal and shearing stresses is shown in Figure 1. Positive normal stresses are tensile and negative normal stresses are compressive. Positive shearing stresses have the directions shown in Figure 1; negative shearing stresses have directions opposite from those shown. The displacements u and v are positive if in the direction of increasing x and y , respectively.

The solution of any two-dimensional elastic problem must satisfy the following equations (Timoshenko and Goodier, 1951, p. 1 f - 27):

For two-dimensional problems, displacements are identical for all xy -cross sections along the z -axis from minus to plus infinity. Positive normal stresses are tensile; negative normal stresses are compressive. Positive shearing stresses have the directions shown; negative shearing stresses are opposite to those shown

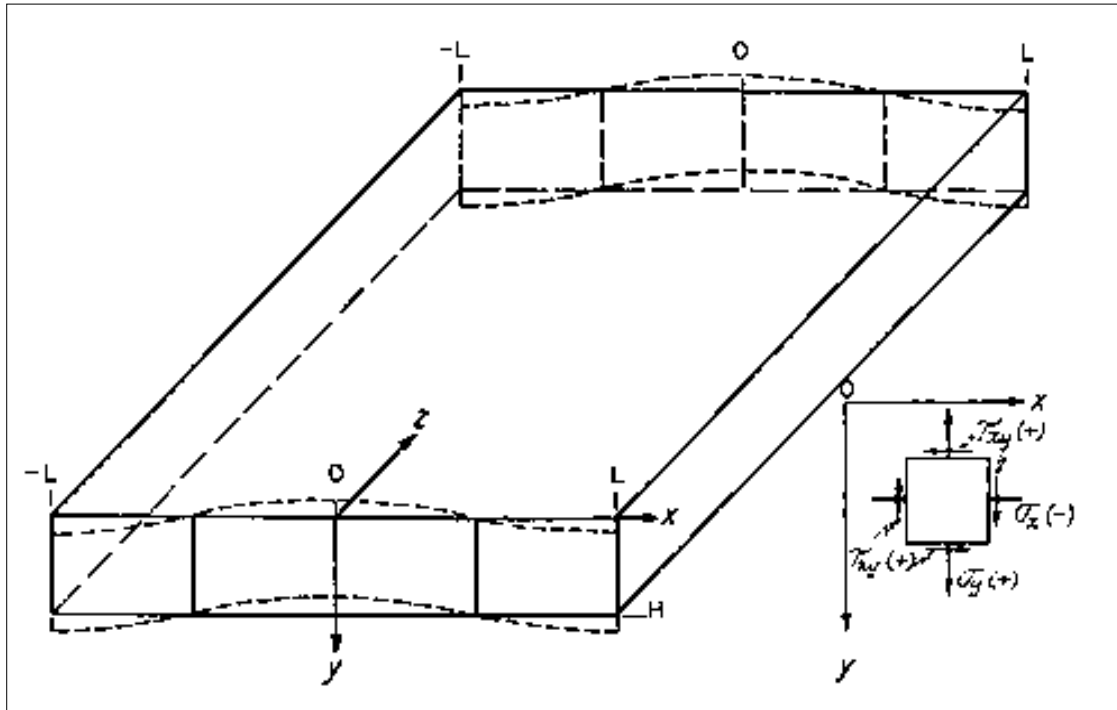


Figure 1. Co-ordinates and Stress Sign Convention for the Elastic Problems

$$\frac{\partial \sigma_x}{\partial x} + \frac{\partial \tau_{xy}}{\partial y} = 0, \quad (1)$$

$$\frac{\partial \sigma_y}{\partial y} + \frac{\partial \tau_{xy}}{\partial x} = 0, \quad (2)$$

$$\nabla^2(\sigma_x + \sigma_y) = 0, \quad (3)$$

(These equations and those which follow omit the terms pertaining to the weight of the layer. The effect of the weight of the layer is incorporated into the solutions in the next section of the text.) Equations (1) and (2) are the differential equations of equilibrium which insure a state of static equilibrium. Equation (3) is the compatibility equation (expressed in terms of stress) which insures a proper relationship between the three components of strain, so that two-dimensional deformation can occur without discontinuities in displacement (Muskhelishvili, 1953, p. 95-97). In addition to satisfying equations (1) through (3), the solution must satisfy specified stress and/or displacement boundary conditions. If the solution of the problem gives stresses and displacements which fulfill all these conditions, then it can be shown that the solution is unique (Timoshenko and Goodier, 1951, p. 236; Muskhelishvili, 1953, p. 66-71).

The stresses in equations (1) through (3) are related to the strains in the following manner:

$$\sigma_x = \lambda \left(\frac{\partial u}{\partial x} + \frac{\partial v}{\partial x} \right) + 2G \frac{\partial u}{\partial x}, \quad (4)$$

$$\sigma_y = \lambda \left(\frac{\partial u}{\partial x} + \frac{\partial v}{\partial x} \right) + 2G \frac{\partial v}{\partial x}, \quad (5)$$

$$\tau_{xy} = G \left(\frac{\partial u}{\partial x} - \frac{\partial v}{\partial x} \right), \quad (6)$$

Rewriting equations (1) through (3) in terms of strains gives:

$$(\lambda + G) \frac{\partial}{\partial x} \left(\frac{\partial u}{\partial x} + \frac{\partial v}{\partial x} \right) + G \nabla^2(u) = 0, \quad (7)$$

$$(\lambda + G) \frac{\partial}{\partial x} \left(\frac{\partial u}{\partial x} + \frac{\partial v}{\partial x} \right) + G \nabla^2(v) = 0, \quad (8)$$

$$\nabla^2 \left[2(\lambda + G) \left(\frac{\partial u}{\partial x} - \frac{\partial v}{\partial x} \right) \right] = 0. \quad (9)$$

The displacements can be expressed as algebraic sums of partial derivatives of a scalar potential $\phi(x, y)$ and a vector potential $\psi(x, y)$, in the following way (Phillips, 1933, p. 186):

$$u = \frac{\partial \phi}{\partial x} + \frac{\partial \psi}{\partial x}, \quad (10)$$

$$v = \frac{\partial \phi}{\partial x} - \frac{\partial \psi}{\partial x}. \quad (11)$$

Substituting derivatives of equations (10) and (11) into equations (7) and (8) gives the equations of equilibrium in terms of the two potentials:

$$(\lambda + 2G) \frac{\partial}{\partial x} (\nabla^2 \phi) + G \frac{\partial}{\partial x} (\nabla^2 \psi) = 0, \quad (12)$$

$$(\lambda + 2G) \frac{\partial}{\partial y} (\nabla^2 \phi) + G \frac{\partial}{\partial y} (\nabla^2 \psi) = 0, \quad (13)$$

Differentiating equation (12) with respect to x and equation (13) with respect to y and adding the two equations gives:

$$\nabla^2(\nabla^2\phi) = 0. \quad (14)$$

Similarly, differentiating equation (12) with respect to y and equation (13) with respect to x and subtracting one equation from the other gives:

$$\nabla^2(\nabla^2\psi) = 0. \quad (15)$$

Equations (14) and (15) require that ϕ and ψ be either harmonic ($\nabla^2\phi = 0$) or biharmonic functions ($\nabla^4\phi = 0$). Substitution of partial derivatives of equations (10) and (11) into the equations for σ_x and σ_y (equations 4 and 5) and summing the results gives:

$$\sigma_x + \sigma_y = 2(\lambda + G)\nabla^2\phi. \quad (16)$$

The sum of σ_x and σ_y is zero when ϕ is a harmonic function. This condition cannot be satisfied by deformed layers (for example, at a free surface where $\sigma_y = 0$ everywhere and σ_x has finite values). Therefore must be a biharmonic function.

The solutions for ϕ and ψ must satisfy the biharmonic differential equations and prescribed boundary conditions. Of interest here is the deformation of an elastic layer of thickness H which has the following stresses and displacements specified on its boundaries:

At $y = 0$, $\sigma_y = 0$, and $\tau_{xy} = 0$ (*stresses zero*);

At $y = H$, $v = -B \cos \alpha x$, and $u = BP \sin \alpha x$,

$$0 \leq P < 1.$$

The lower surface of the layer undergoes vertical and horizontal displacements proportional to the $\cos \alpha x$ and $\sin \alpha x$, respectively. Assume that the vertical and horizontal displacements within the layer are also proportional to the $\cos \alpha x$ and $\sin \alpha x$. Equations (10) and (11), which expresses displacements in terms of the potential functions, indicates that the above distribution of displacements may be possible with potential functions of the form:

$$\phi = \cos \alpha x F(y), \quad (17)$$

$$\psi = \sin \alpha x f(y), \quad (18)$$

At this point, there is no guarantee that equations (17) and (18) will lead to a solution of the problem. Equations (17) and (18) are the correct expressions for the potential functions only if the stresses and displacements derived from them satisfy equations (1) through (3) and the prescribed boundary conditions.

$F(y)$ and $f(y)$ can be determined by substituting equations (17) and (18) into equations (14) and (15) and solving the resulting fourth-order differential equations. This leads to general expressions for ϕ and ψ .

$$\phi = \cos \alpha x [A_1 e^{\alpha y} + A_2 y e^{\alpha y} + A_3 e^{-\alpha y} + A_4 y e^{-\alpha y}], \quad (19)$$

$$\psi = \sin \alpha x [A_5 e^{\alpha y} + A_6 y e^{\alpha y} + A_7 e^{-\alpha y} + A_7 y e^{-\alpha y}], \quad (20)$$

Where A_1 through A_8 are arbitrary constants.

Equations (19) and (20) contain eight arbitrary constants, whereas only four boundary conditions are specified in the problem. Four extra-arbitrary constants appear in the equations for the potential functions as a result of (1) expressing the displacements as partial derivatives of potential functions (equations 10 and 11), and (2) differentiating the equations of equilibrium to obtain the two biharmonic equations. Some of the constants in the general expressions for ϕ and ψ are related. Substituting equations (19) and (20) into equations (12) and (13) gives:

$$A_6 = \left(\frac{\lambda+2G}{G}\right) A_2 = \frac{2(1-\nu)}{1-2\nu} A_2 = K_1 A_1, \quad (21)$$

$$A_8 = \left(\frac{\lambda+2G}{G}\right) A_4 = -\frac{2(1-\nu)}{1-2\nu} A_4 = -K_1 A_4, \quad (22)$$

These relationships eliminate two of the extra constants.

The remaining two extra constants were eliminated by trial and error until equations for ϕ and ψ were found which satisfied the four boundary conditions and the equations of equilibrium and compatibility. The equations for ϕ and ψ satisfying the requirements for a solution of stress and strain in the elastic layer are:

$$\phi = \cos \alpha x [A_1 (e^{\alpha y} + e^{-\alpha y}) + A_2 y e^{\alpha y} + A_4 y e^{-\alpha y}], \quad (23)$$

$$\psi = \sin \alpha x [A_5 (e^{\alpha y} + e^{-\alpha y}) + K_1 A_2 y e^{\alpha y} + K_1 A_4 y e^{-\alpha y}], \quad (24)$$

The constants in the above equations are equal to:

$$A_1 = 0,$$

$$A_2 = \frac{B\alpha C_2}{N} = \frac{B\alpha}{N} \{K_3 [(1-P)e^{\alpha H} - (1-P)(1+2\alpha H)e^{-\alpha H}] - 2(K_1 - P)e^{-\alpha H}\}, \quad (25)$$

$$A_4 = \frac{B\alpha C_4}{N} = \frac{B\alpha}{N} \{K_3 [(1+P)e^{-\alpha H} - (1-P)(2\alpha H - 1)e^{\alpha H}] - 2(K_1 + P)e^{\alpha H}\}, \quad (26)$$

$$A_5 = \frac{BC_5}{N} = -\frac{BK_3}{N} [(K_1 + \alpha H P K_3)(e^{\alpha H} + e^{-\alpha H}) + (P - \alpha H K_3)(e^{\alpha H} - e^{-\alpha H})], \quad (27)$$

where

$$N = \alpha N_1 = \alpha [K_3 (2 - e^{2\alpha H} - e^{-2\alpha H}) - K_1 K_3 (2 + e^{2\alpha H} + e^{-2\alpha H}) + 4\alpha^2 H^2 K_3^2 + 4K_1], \quad (28)$$

and

$$K_3 = (1 - K_1) = -\frac{1}{1-2\nu}. \quad (29)$$

The general equations for v , u , σ_y , σ_x and τ_{xy} are

$$v = \frac{B \cos \alpha x}{N_1} [C_2 e^{\alpha y} (\alpha y K_3 + 1) C_4 e^{-\alpha y} (\alpha y K_3 - 1) - C_5 (e^{\alpha y} + e^{-\alpha y})], \quad (30)$$

$$u = \frac{B \sin \alpha x}{N_1} [-C_2 e^{\alpha y} (\alpha y K_3 + K_1) - C_4 e^{-\alpha y} (\alpha y K_3 - K_1) + C_5 (e^{\alpha y} + e^{-\alpha y})], \quad (31)$$

$$\sigma_y = \frac{2GB\alpha \cos \alpha x}{N_1} [C_2 K_3 \alpha y e^{\alpha y} - C_4 K_3 \alpha y e^{-\alpha y} - C_5 (e^{\alpha y} - e^{-\alpha y})], \quad (32)$$

$$\sigma_x = -\sigma_y + \frac{2GB\alpha \cos \alpha x}{N_1} [-2K_3 (C_2 e^{\alpha y} - C_4 e^{-\alpha y})], \quad (33)$$

$$\tau_{xy} = \frac{2GB\alpha \sin \alpha x}{N_1} [C_5 (e^{\alpha y} + e^{-\alpha y}) - C_2 K_3 e^{\alpha y} (\alpha y + 1) + C_5 K_3 e^{-\alpha y} (\alpha y - 1)], \quad (34)$$

Also of interest in elastic analysis are the equations for the principal stresses. The principal stresses at a point within a stressed layer are the stress values normal to three perpendicular planes across which the shearing stresses vanish. In a two-dimensional analysis, the intermediate principal stress (σ_2) parallels the z -axis. The equations for the principal stresses in terms of σ_x , σ_y , and τ_{xy} are:

$$\sigma_1 = \frac{\sigma_x + \sigma_y}{2} + \sqrt{\left(\frac{\sigma_x - \sigma_y}{2}\right)^2 + \tau_{xy}^2}, \quad (35)$$

$$\sigma_3 = \frac{\sigma_x + \sigma_y}{2} - \sqrt{\left(\frac{\sigma_x - \sigma_y}{2}\right)^2 + \tau_{xy}^2}, \quad (36)$$

The response of an elastic layer to general distributions of displacement along its lower boundary can be determined by superposing equations of the type which have been shown herein (Timoshenko and Goodier, 1951, Kennedy, B. Stix Vallance, J.W. Lavalley, V and Longpre, M.A. 2004). Combination of equations is accomplished by means of a Fourier series, which can be used to approximate a variety of geologically reasonable displacements at the base of a sedimentary layer.

Superposition can also be used to incorporate into the equations an initial state of stress due to the weight of the layer. In this work, a state of hydrostatic stress:

$$\sigma_x = -\rho g y, \sigma_y = -\rho g y, \text{ and } \tau_{xy} = 0,$$

Which satisfies the equilibrium and compatibility requirements, has been superposed with stresses arising from the deformation of the layer. This superposition of equations gives the correct stress values for layers which are assumed to be in hydrostatic equilibrium prior to deformation Faller, A.M. and Soper, N.J., 1979)

Application of analytical method to examples

The internal stress distribution of a deformed elastic layer can be portrayed by a set of orthogonal curves called stress trajectories. These stress trajectories are tangent to the directions of the principal stresses at all points within the layer. The equation for the direction of one of the principal stresses (σ_1 or σ_2) in the two-dimensional case is:

$$\tan 2\beta = \frac{2\tau_{xy}}{\sigma_x - \sigma_y}, \quad (37)$$

where β is the angle between the positive x -axis and the principal stress measured in the direction of the positive y -axis. In the numerical examples discussed in following sections, a graphical

construction of the stress trajectories was made on the basis of β values computed for a grid of points within the layer.

The only factors which influence the orientations of the stress trajectories are the shape of the layer (ratio of H to L) and Poisson's ratio. Rigidity (G), maximum applied vertical displacement (B), and hydrostatic stress cancel out of equation (37). The shape of the layer (H/L) and Poisson's ratio appear in the stress equations through the constants K_1, K_3, C_2, C_4 and C_5 .

The distribution of displacement in a deformed layer can be portrayed by a field of displacement vectors. The orientation and length of each vector indicate the direction and magnitude of the net displacement at the point from which the vector originates. (Vendeville, B,1991)

The only factors which influence the orientations and relative magnitudes of the displacement vectors are the shape of the layer and Poisson's ratio. Rigidity (G) does not appear in the displacement equations. The shape of the layer (H/L) and Poisson's ratio enter into the displacement expressions through K_1, K_3, C_2, C_4 and C_5 .

Stress distributions and displacement fields of different examples can be compared if each numerical example sustains an amount of applied displacement which is just necessary to initiate fracture at some point within the layer. In the numerical examples which follow, displacements necessary to initiate fracture were computed on the basis of a special case of the Mohr fracture criterion.

The equation for this fracture criterion is:

$$\tau = \tau_0 - \sigma \tan \phi, \quad (38)$$

where τ and σ are the shearing and normal stresses across a potential fracture plane, τ_0 is the shear stress necessary to overcome the initial shear strength due to cohesion, and ϕ is the angle of internal friction. The shear strength is dependent on the type of stress (tensile or compressive) and the amount of confining (hydrostatic) stress. The criterion is diagrammed in Figure 2.

This special form of the Mohr criterion was selected because it satisfactorily describes the shear strength of many sedimentary rocks under the confining pressures encountered at depth in sedimentary basins ($1000 - 2000 \text{ kg/cm}^2$) (Jaeger, 1956, p.82). For zero or low confining pressures, the criterion may not explain tensile fracture of rock subjected to tensile stress. Inasmuch as present experimental data are inadequate for establishing a fracture criterion for rocks under tension, the assumption was made that the Mohr criterion does describe fracture under tensile stresses.(Barriere ,M.1977).

Critical displacements in the numerical examples were determined as follows:

1. Principal stresses were found for a grid of points by substituting computed values of σ_x, σ_y and τ_{xy} into equations (35) and (36). However, in computing these stresses, B (which appears in the equations for σ_x, σ_y and τ_{xy}) was not given a value. By carefully examining these computed principal stresses, all but a few points in the layer could be eliminated as probable points of fracture.
2. A displacement (B) necessary to initiate fracture at each of the probable points of fracture was found by substituting the values of the principal stresses (expressed as

fractions of B plus a hydrostatic stress term) into a rearranged form of equation (38):

$$\left| \frac{\sigma_1 - \sigma_3}{2} \right| = \tau_0 \cos \phi - \left(\frac{\sigma_1 + \sigma_2}{2} \right) \sin \phi, \quad (39)$$

and solving for B .

3. The point giving the smallest value of B was selected as the point of fracture, and the computed B was taken as the critical displacement B_c .

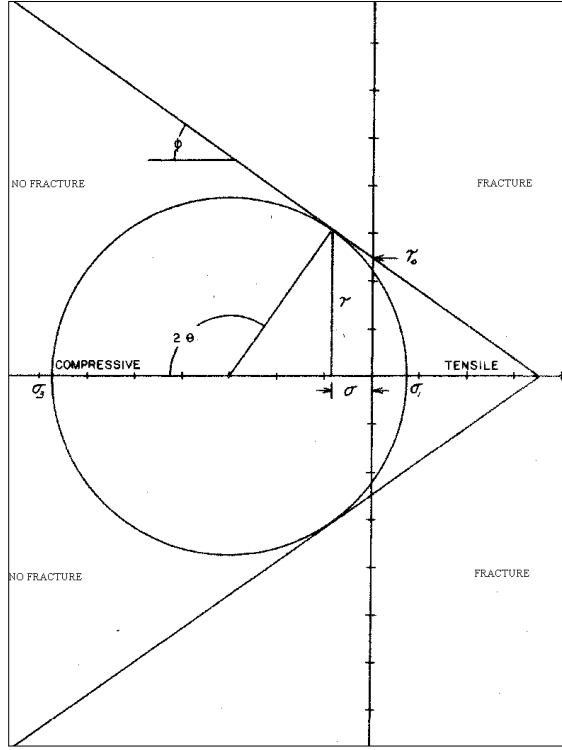


Figure 2. Diagram of the Mohr Fracture Criterion

The Mohr criterion explains satisfactorily the shear strength of brittle materials which are generally elastic up to the point of fracture. However, some materials, after an initial period of elastic deformation, yield by plastic flow rather than by fracture. In the elastic region of the deformation, the analysis of stress and displacement is the same regardless of the type of failure which occurs. The initiation of plastic flow, however, τ and σ are the shearing and normal stresses across a potential fracture plane, τ_0 is the shear strength due to cohesion, ϕ is the angle of internal friction, and θ is the angle between the stress trajectory and the line of fracture is probably controlled by a different condition than fracture in brittle substances (Langston, C.A., 1971). Flow is believed to occur when the strain energy of distortion per unit volume reaches a value characteristic of the material (Jaeger, 1956, P.93). The formula for this criterion in the two-dimensional plane strain case is (Timoshenko and Goodier, 1951, p. 149):

$$E_d = \frac{1}{12G} \left\{ [\sigma_x - \sigma_y]^2 + [\sigma_y - \nu(\sigma_x + \sigma_y)]^2 + [\nu(\sigma_x + \sigma_y) - \sigma_x]^2 + 6\tau_{xy}^2 \right\}, \quad (40)$$

This criterion, credited to R. von Mises, differs from the Mohr criterion in that initiation of plastic flow is independent of confining stress and occurs regardless of whether the stresses are tensile or compressive.

In the numerical examples, values of distortional strain energy density were calculated using the values of stress dictated by the Mohr fracture criterion. The values obtained in this manner are not related to any characteristic values for rock materials. However, the distributions of distortional strain energy density do show the regions susceptible to flow in materials which favor this mode of failure (Marti, J. Ablay, G.J., Redshaw, L.T. and Sparks, R.S.J. 1994).

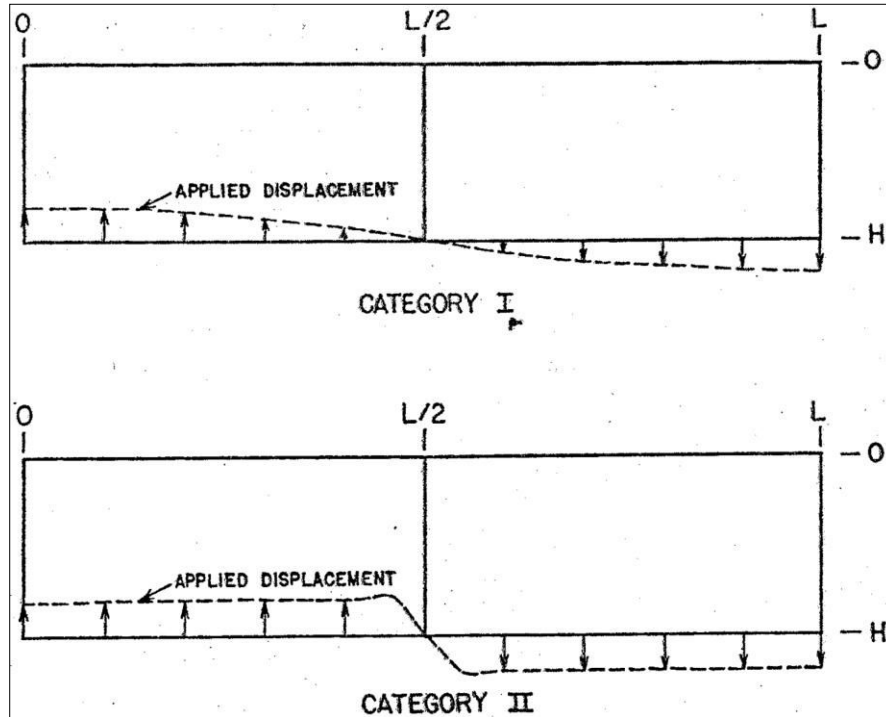


Figure 3. Classification of Numerical Examples Applied vertical displacement in Category I is sinusoidal; applied vertical displacement in Category II is an approximate step.

Numerical examples

Introduction –

Table 1 summarizes the numerical calculations. The examples are categorized according to the nature of the displacement specified along the lower boundary of the elastic layer (Figure 3). In Category I, the lower boundary of an elastic layer undergoes sinusoidal vertical displacement and no horizontal displacement. Equations (25) through (34) (with $P = 0$) were used for the numerical examples in the first category. In Category II, the lower boundary of an elastic layer undergoes an approximate step in vertical displacement and no horizontal displacement. Eight solutions of the type given by equations (25) through (34) (with $P = 0$) were superposed by means of a Fourier series to obtain the numerical example in this category. In Category III, the lower boundary of an elastic layer undergoes sinusoidal vertical and horizontal (90° out of phase with the vertical) displacements. Equations for the numerical example in this category are given in a later section.

The boundary conditions at the upper surface of the elastic layer are $\sigma_y = 0$ and $\tau_{xy} = 0$. These conditions specify a free upper surface which corresponds to the surface of the earth (Allen, C.R., Amann, P., St. Richter, C.F. and Nordquist, J.M. 1965). In Categories I and II, the boundary conditions on the lower surface are (1) no horizontal displacement and (2) a specified distribution of vertical displacement. The latter conditions approximate the situation along the lower τ and σ are the shearing and normal stresses across a potential fracture plane, τ_0 is the shear strength due to cohesion, ϕ is the angle of internal friction, and θ is the angle between the stress trajectory and the line of fracture. Surface of an elastic sedimentary layer which is deformed by vertical movement of rigid bedrock beneath it. The contact between rigid bedrock and elastic sedimentary rock is "welded" so that horizontal movement along the contact is prevented.

Average values of the properties of sedimentary rocks are used in each example. The density, 2.5 gms/cm^3 , and Poisson's ratio, 0.25, are based on the values listed in Birch et al. (1942, P.8-37, 76). The rigidity value Adopted, $2.0 \times 10^{11} \text{ dynes/cm}^2$, is Gutenberg's estimate of rigidity for Tertiary sandstone at a pith of 2 km (Gutenberg, 1951, p. 367). The angle of internal friction, 35° , is based on experimental evidence cited by Hubbert (1951). The cohesive strength, 250 kg/cm^2 , was calculated from crushing-strength data on sedimentary rocks (Birch et al., 1942, P.116; Marin, 1952, P. 381; Mills et al., 1955, P. 310) and the adopted angle of internal friction of 35° .

Results of the numerical calculations are diagrammed in Figures 4-6 and 10. These figures are drawn for a short portion of a layer between the limits $x = 0$ and $x = L$. However, the symmetry of the problem permits visualization of results for longer layers if the drawings are rotated 180° about vertical axes in the plane of the figure.

The displacements shown in these figures are only those resulting from the application of vertical displacements on the lower boundary of the layer. The stress values, on the other hand, include the initial hydrostatic stresses as well as the stresses arising from the deformation of the layer. (Couples, G.D., Lewis, H., Olden, P., Workman G.H. and Higgs, G. 2007)

Category i examples - Displacement fields for Category I examples are shown in Figures 4 A and 5 A. Theoretically, two factors influence the relative magnitudes and orientations of the displacement vectors in these figures the dimensions of the layer and Poisson's ratio. Figure 7 shows the relative changes in the maximum displacements at the boundaries with changes in these factors. The shape of the layer has a strong influence on the displacement field, whereas Poisson's ratio has little effect.

The stress distributions for Category.1, examples are shown in Figures 4 B and 5 B. The orientations of the stress trajectories in these figures are determined by the shape" of the layer (H/L) and Poisson's ratio. Comparison of Figures 45 and 55 shows the influence of shape on the direction of the stress trajectories. Stress distributions calculated for two other examples (layer dimensions same as Figure 45) with Poisson's ratios of 0.167 and 0.333 were nearly identical in appearance. Between these two values, orientation of stress trajectories is nearly independent of variations in Poisson's ratio. Of interest in the stress diagrams (Figs. 4B and 5B) is the area of horizontal tensile stress centered over the crest of the deformed layer and extending to a depth of approximately 1 kilometer . Inasmuch as rocks are very weak Funder "tensile stress, point F on Figures 4 B and 5 B, where the tensile stresses are greatest, is the point of initial fracture. For brittle rock, the type of fracture under the stress conditions at F is a vertical crack (Jaeger, 1956,

p. 74). The maximum applied displacement or critical displacement before fracture occurs at F in Figures 45 and 55 is 8.2 and 4.5 m respectively.

Two regions are equally susceptible to yielding by plastic flow according to the distortional strain-energy density distributions in Figures 4C and 5C. One region is centered over the crest of the deformed layer, the other is centered in the trough of the deformed layer (Couples G.D. and Lewis, 1999). The high distortional strain-energy at the crest of the fold reaches a maximum value at the point of fracture determined by the Mohr criterion. Fracture does not occur in the other region of high distortional strain-energy, inasmuch as the compressive stresses in this region are insufficient to initiate fracture according to the Mohr criterion.

Category ii example –

Figure 6 A shows the displacement field for the Category II example. The influence of layer shape on the maximum displacements at the boundaries is given in Figure 8. Figure 6 B shows the stress distribution for the Category II example. Two features are notable. First, most of the vertical stress along the bottom of the layer is concentrated toward of the adjoining uplifted and down dropped blocks. Second, the stresses in the central regions of the uplifted and down dropped blocks are nearly zero if initial hydrostatic stresses are disregarded. Both these features indicate that deformation of the layer is restricted to the region where the two blocks meet. In addition, the lack of stress in the central regions of the layer indicates that a uniform displacement superposed on any of the examples will not change the stress distribution. Therefore the results shown in Figures 4 B, 5 B and 6 B are also solutions for examples in which all vertical displacements applied along the lower boundary are in one direction.(Murdock, J.N.1979, McClay, K.R. 1990, Barriere , m.1977)

The same applied displacement will cause fracture at F_2 ($x = 0.53L, y = H$) as well as F_1 if the fracture properties (τ_0 and ϕ) of the layer are changed. Figure 9 shows the conditions under which fracture will occur simultaneously at F_1 and F_2 . The stresses at F_2 are compressive in both the x – and y –directions. The type of failure for brittle rock under these stress conditions is a shear fracture (Yin, H. and Groshong, R.H. Jr, 2007)

Two separate regions of high distortional strain-energy density occur along the upper boundary of the layer (Figure 6 C). The maximum value in each of these regions is equal to the maximum values found in the Category I examples. The highest distortional strain-energy concentration occurs at the bottom of the layer directly above the point at which the rate of change of applied displacement is greatest.

In Figure 65, a region of nearly horizontal tensile stress lies just to the left of $x = L/2$, $y = 0$ and extends to a maximum depth of 1 *kilometer*. The point of initial fracture (F_1) is at $x = 0.375L$, $y = 0$, where these tensile stresses are greatest. The type of fracture under the stress conditions at F_1 is a vertical tensile crack. The amount of applied vertical displacement required to initiate fracture at F_1 is 3.7 m .

Scope of numerical examples in categories i and ii - Theoretically, two factors influence the orientations of the displacement vectors and the stress trajectories the dimensions of the layer and Poisson's ratio. The calculations which have been described indicate that layer shape has a strong influence on these orientations, whereas Poisson's ratio has little effect. As a result, the numerical solutions given here are applicable to any homogeneous elastic layer providing (1) its shape is the same as the shape of the layer in the example, and (2) an appropriate scaling factor is used to

determine the magnitudes of stress in the stress diagram. The scaling factor is based on the rigidity of the layer and the maximum applied displacement. The maximum applied displacement must be less than the amount of displacement necessary to initiate fracture.

TABLE 1.—SUMMARY OF THE NUMERICAL EXAMPLES

Boundary Conditions	Category I		Category II	Category III
	At $y = 0$	$\sigma_y = 0; \tau_{xy} = 0$	$\sigma_y = 0; \tau_{xy} = 0$	$\sigma_y = 0; \tau_{xy} = 0$
	At $y = H$	$v = -B \cos \frac{\pi x}{L}; w = 0$	$v = \frac{4B}{\pi} \sum_{n=1}^8 \frac{(-1)^{n+1}}{(2n-1)} \cos(2n-1) \frac{\pi x}{L}; u = 0$	$\sigma_y = -A \sin \frac{\pi x}{L}; \tau_{xy} = 0$
Examples	Ia	Ib	IIa	IIIa
1. Dimensions of layer				
H —km	5	5	5	5
L —km	25	15.7	25	15.7
2. Elastic properties				
ν —Poisson's ratio	0.25	0.25	0.25	0.25
G — 10^{11} dynes/cm ²	2.0	2.0	2.0	2.0
3. Fracture properties				
ϕ —degrees	35	35	35	35
τ_0 —kg/cm ²	250	250	250	250
4. Fracture point location				
x	0	0	0.375L	L/2
y	0	0	0	0
5. Magnitude and location of maximum stresses				
σ_x —kg/cm ²	-1261	-1275	-1578	-1508
x	0	0	0.45L	L/2
y	H	H	H	H
σ_y —kg/cm ²	-1282	-1324	-2229	-1292
x	0	0	0.45L	L/2
y	H	H	H	H
τ_{xy} —kg/cm ²	74	103	489	63
x	L/2	L/2	L/2	0
y	H	H	H	H/2
6. Magnitude and location of maximum displacements at the upper boundary				
v —meters	7.8	3.9	3.7	5.7
x	0	0	0	L/2
u —meters	3.8	2.4	3.0	2.5
x	L/2	L/2	L/2	0
7. Magnitude and location of maximum displacements at the lower boundary				
v —meters	8.2	4.5	3.7	5.8
x	0	0	—	L/2
u —meters	0	0	0	2.4
x	—	—	—	0

Elastic properties of the layer do not have to be known for a comparison of elastic analyses and scale-model experiments (Sharp, I.R. Gawthorpe, R.L. Underhill, J.R.2000).

Displacements and fractures (see "Prediction of fractures"), the only items easily observed in model experiments, are independent of the' elastic constants in the elastic analyses.

Therefore, geometrical similarity of layer shapes is the only requirement for a comparison between a two-dimensional elastic analysis and a two-dimensional scale model.

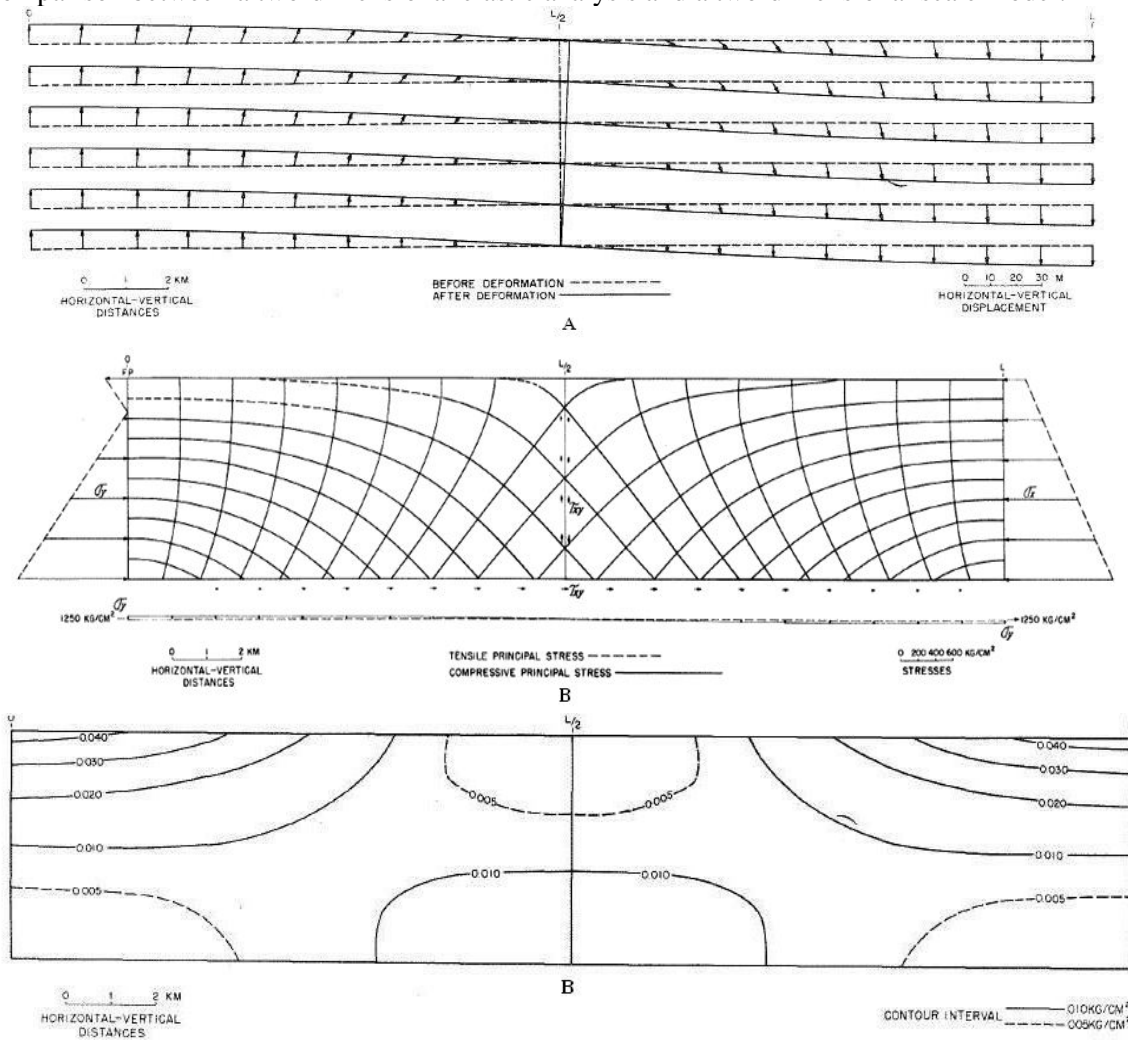


Figure 4. Example Ia Diagrams: A-Displacement Field; B-Stress Distribution; C-Distortional Strain-Energy Density In example Ia, the lower boundary of an elastic layer 5 kilometer thick and 25 kilometer long undergoes half a wave length of sinusoidal vertical displacement.

Category iii example - A "welded" contact, which is specified along the lower boundary in Categories I and II examples, is one extreme of many possible contact conditions. The opposite extreme is a "frictionless" contact. The frictionless lower-boundary case was analytically investigated to determine the effect of contact conditions on deformation resulting from a sinusoidal distribution of vertical displacement

A frictionless condition at the lower boundary means that the shearing stress is zero along that boundary. The magnitude of applied horizontal displacement which gives zero shearing stress along the lower boundary is difficult to compute. The easiest approach is to specify stresses on the lower boundary as Hafner (1951) did in his work.

The solution of problems in which all boundary conditions are expressed in terms of stress reduces to the solution of a single biharmonic equation which will lead to stresses satisfying equilibrium (equations 1 and 2), compatibility (equation 3), and the prescribed boundary conditions. Of interest here is the deformation of an elastic layer of thickness H under the following boundary conditions:

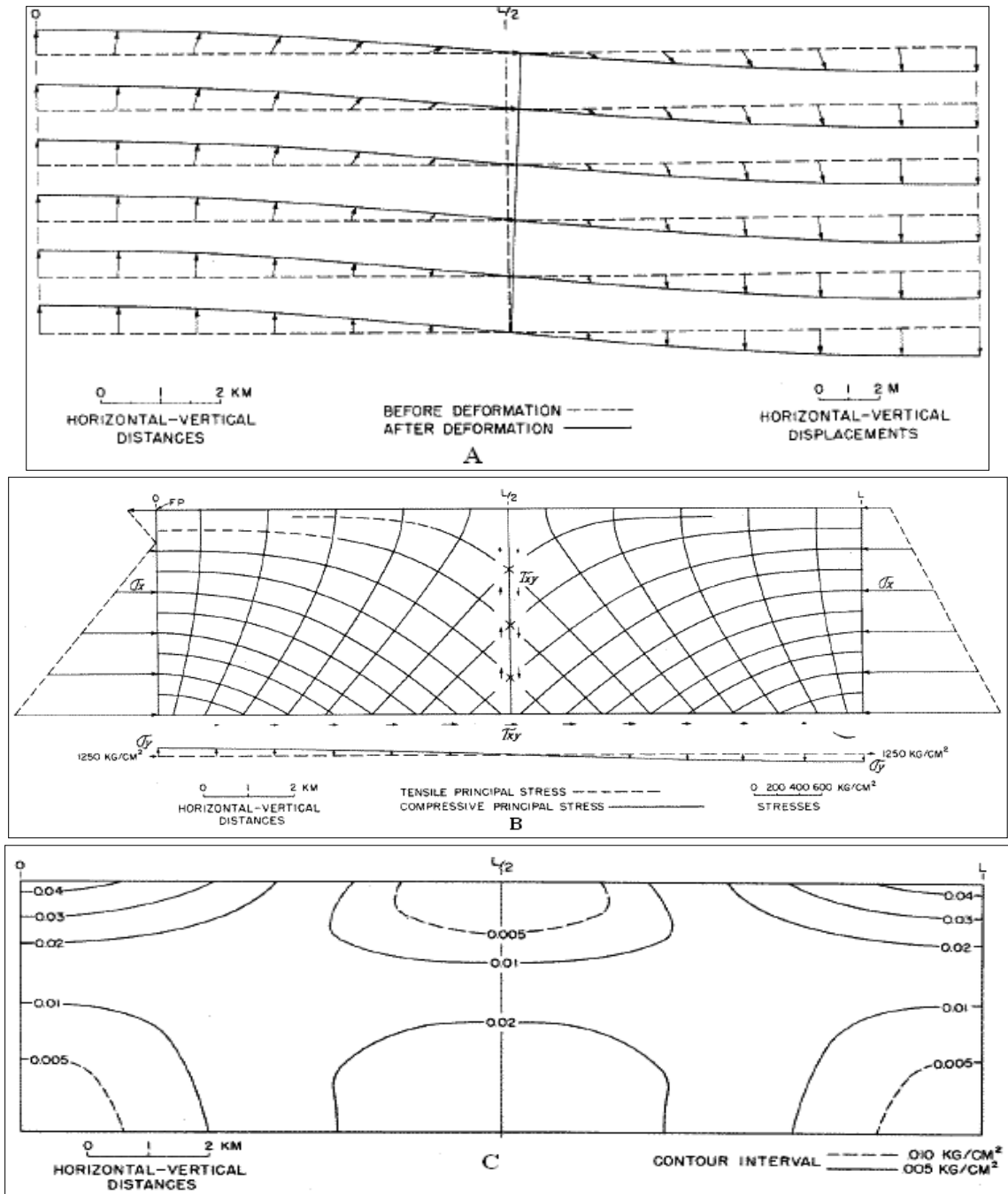


Figure 5. Example Ib Diagrams: A -Displacement Field; B - Stress Distribution; C - Distortional Strain-Energy Density. In example Ib, the lower boundary of an elastic layer **5 km** thick and **15.7 km** long undergoes half a wave length of sinusoidal vertical displacement.

At $y = 0, \sigma_y = 0, \tau_{xy} = 0$ (stresses zero);
 At $y = H, \sigma_y = -A \sin \alpha x, \tau_{xy} = 0$.

The biharmonic equation and the boundary conditions are satisfied by:

$$\phi = \sin \alpha x [D_1 \cos h\alpha y + D_2 \sin h\alpha y + D_3 y \cos h\alpha y + D_4 y \sin h\alpha y], \quad (41)$$

The constants in equation (41) are equal to:

$$D_1 = 0,$$

$$D_2 = -\frac{D_3}{\alpha} = \frac{D_4 k_1}{\alpha} = \frac{D_4}{\alpha} \left[\frac{\sin h\alpha H + \alpha H \cos h\alpha H}{\alpha H \sin h\alpha H} \right], \quad (42)$$

$$D_3 = -D_4 k_1 = -D_4 \left[\frac{\sin h\alpha H + \alpha H \cos h\alpha H}{\alpha H \sin h\alpha H} \right], \quad (43)$$

$$D_4 = \frac{A}{\alpha k_2} = \frac{A}{\alpha [(\alpha H + k_1) \sin \alpha H - k_1 \alpha H \cos \alpha H]}, \quad (44)$$

The general equations for $\sigma_y, \sigma_x, \tau_{xy}, v$, and u are:

$$\sigma_y = -\frac{A \sin \alpha x}{k_2} \cdot [(\alpha y + k_1) \sin h\alpha y - \alpha y k_1 \cos h\alpha y], \quad (45)$$

$$\sigma_x = \frac{A \sin \alpha x}{k_2} \cdot [(\alpha y - k_1) \sin h\alpha y + (2 - \alpha y k_1) \cos h\alpha y], \quad (46)$$

$$\tau_{xy} = -\frac{A \cos \alpha x}{k_2} \cdot [(1 - \alpha y k_1) \sin h\alpha y + \alpha y \cos h\alpha y], \quad (47)$$

$$v = \frac{A \sin \alpha x}{2\alpha G k_2} [(1 - 2\nu) \sin h\alpha y + \alpha y k_1 \sin \alpha y - 2k_1(1 - \nu) \cos h\alpha y - \alpha y k_1 \cos \alpha y] + \text{constant}, \quad (48)$$

$$u = -\frac{A \cos \alpha x}{2\alpha G k_2} [-k_1(1 - 2\nu) \sin h\alpha y + \alpha y \sin h\alpha y + 2(1 - \nu) \cos h\alpha y - \alpha y k_1 \cos \alpha y - \alpha y k_1 \cos h\alpha y] + \text{constant}, \quad (49)$$

The elastic constants appear in the displacement equations, but not in the stress equations.

Table 1 summarizes the results obtained from numerical example IIa. In example IIa, a sinusoidal vertical stress is applied to the lower boundary of an elastic layer. The elastic constants and fracture properties for the layer are the same as in the previous examples. The results of the calculations are diagrammed in Figure 10. In addition, calculations were made to determine the influence of layer shape on the relative magnitudes of maximum displacement at the boundaries (Figure 11). Fracture point and critical displacement were determined by the Mohr fracture criterion (equations 38 and 39).

A comparison of examples III a and I b shows the maximum influence of the conditions at the flower boundary on the deformation resulting from a sinusoidal distribution of applied vertical displacement. The layers in these examples have identical dimensions, elastic constants, and fracture characteristics. Both undergo the same distributions of vertical displacement along

the lower boundary. The only difference is the contact between the layer and underlying material. Example III a has a frictionless contact, and example Ib has a welded contact.

The following are not greatly affected by the nature of the contact:

1. The point of initial fracture as determined by the Mohr criterion (compare position of F on Figure 5 B and 10 B).
2. The distribution of vertical and horizontal displacements at the upper boundary as a function of the dimensions of the layer (compare Figure 7 A and 11).

The features which change when the lower boundary is frictionless are:

1. The amount of applied vertical displacement before fracture is slightly greater.
2. Two additional areas are susceptible to yielding by plastic flow (compare Figure 5 C and 10 C).
3. Horizontal displacements nearly equal to those on the upper boundary occur along the lower boundary (compare Figure 5 A and 10 A).

If displacement does occur along the lower contact of a layer, it will always be less than the amount found in example III a. An absolutely frictionless contact between rock layers is not a reasonable boundary condition in geologic problems. For this reason, most features of the deformation in a homogeneous layer will tend to be closer to those occurring in the "welded" contact case.

Prediction of fractures

According to the Mohr criterion, fracture occurs along lines which intersect the principal stresses at constant angles. The angle between the line of fracture and the stress trajectories is equal to (Figure 2)

$$\theta = 45^\circ \pm \frac{\phi}{2}, \quad (50)$$

The extent to which the stress distributions in the analytical work can be used in predicting fractures with the Mohr criterion is difficult to determine. Any fracturing within the layer changes the stress distribution determined in the elastic analysis. If this change is confined to regions near the fracture, then formation and propagation of fractures are controlled by the original stress distribution. On the other hand, if the change extends a large distance from the fractures, formation and propagation of fractures are controlled by a stress distribution which changes continuously as the fractures are formed. One method of determining whether or not stress distributions from an elastic analysis can be used to predict fractures is to perform experiments.

Experimental Study

Problems investigated

Two problems similar to the analytical examples were investigated in the scale-model experiments. The first dealt with the deformation of a homogeneous layer resulting from the application of a broad curve in vertical displacement along its lower boundary. The second problem dealt with the deformation of a homogeneous layer resulting from the application of a step in vertical displacement along its lower boundary.

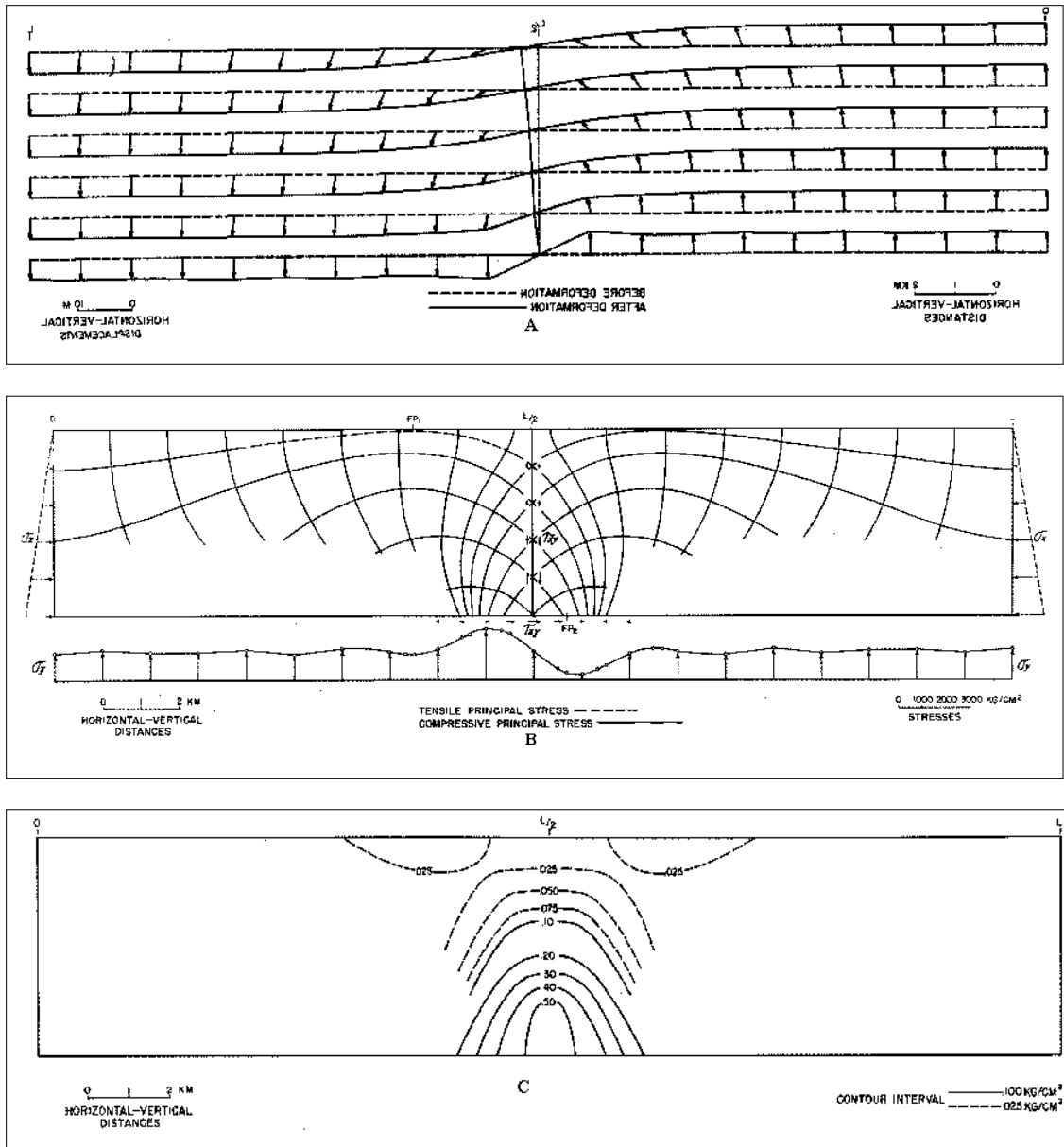


Figure 6. Example IIa Diagrams: A-Displacement Field; B-Stress Distribution; C-Distortional Strain-Energy Density

Theory

Only the scale-model theory needed for this discussion is summarized here. A more detailed account of scale-model theory and its application to geologic problems is given by Hubbert (1937). A geologic structure and a scale-model representation of the same structure must have certain similarities. The model must be similar in shape to the geologic structure; that is, lengths, areas, and volumes must be proportional.

$$L_m = \lambda L_n,$$

$$A_m = \lambda^2 L_n^2, \tag{51}$$

$$V_m = \lambda^3 L_n^3,$$

(Subscripts **m** and **n** indicate model and nature, respectively.) The mass distributions must be similar; that is, the mass for any element of volume in the model must be proportional to the mass of the corresponding element in the geologic structure:

$$dM_m = \mu dM_n, \quad (52)$$

The time required for any given change of shape or position in the model must be proportional to the time required in the geologic structure:

$$T_m = \tau T_n, \quad (53)$$

The constants of proportionality in these equations, λ , μ and τ are the model ratios of length, mass, and time, respectively. From these model ratios, it can be seen that dynamic similarity between the model and the original exists if the ratio of each force acting on an element of mass in the model is proportional to the same force acting on the corresponding element of mass in the geologic structure:

$$\frac{dM_m L_m T_m^{-2}}{dM_n L_n T_n^{-2}} = \mu \lambda \tau^{-2} = \phi, \quad (54)$$

In the formation of geologic structures and also in the modeling of these structures, accelerations are generally so small that forces due to inertia are negligible. If inertia forces are negligible, dynamic similarity is completely satisfied (for independent values of the model ratios λ , μ and τ) as long as all forces conform to the model ratio of the gravity forces (Hubbert, 1937, p. 1489). The geologic structure and the model are subjected to the same gravitational field, therefore, the model ratio of gravity force is:

$$\frac{F_m}{F_n} = \frac{dM_m g}{dM_n g} = \mu, \quad (55)$$

From equation (55) the ratio of strength between the model and the original structure is derived:

$$\sigma = \mu \lambda^{-2}, \quad (56)$$

The model ratio of mass can be expressed as:

$$\mu = \delta \lambda^3, \quad (57)$$

where δ equals model ratio of density. Substituting equation (57) into equation (56) gives for the model ratio of strength:

$$\sigma = \delta \lambda, \quad (58)$$

Replacing λ with the ratio of lengths gives:

$$L_n = \frac{\delta L_m}{\sigma}, \quad (59)$$

Equation (59) can be used to establish the size of the geologic structure being modeled if the model ratios of strength and density are known.

Description of experiments

Properties of modelling materials –

The composition of the materials used in the experiments was:

Material 1	Beach sand
Material 2	Beach sand 85 per cent, clay 15 per cent (QM-4 Kentucky-Tenn. Clay Co.)
Material 3	Coarse St-Peter sand (Ottawa Silica / Sands, flint shot)
Material 4	Fine St—Peter sand (Ottawa Silica Sands, #102)

Density values for the two degrees of compaction used in the experiments were:

	<i>Uncompacted</i>	<i>Compacted</i>
Material 1	1.3 gms/cm ³	1.6 gms/cm ³
Material 2	1.3gms/cm ³	1.7 gms/cm ³
Material 3	1.5gms/cm ³	1.7 gms/cm ³
Material 4	1.4gms/cm ³	1.7 gms/cm ³

Figure show, relative change in maximum displacements at layer boundaries with change in layer dimensions. The first value is an average density for the material, when it is poured into a container. The second value is an average density for the material when moderately tamped (at approximately 10,000 *dynes/cm*²).

No water was added to any of the materials used. However, a small percentage of moisture was absorbed from the air. Water-content measurements showed that (1) 2.4 per cent of weight of the clay in Material 2 was rater/and (2) 0.9 **percent** of the total weight of Material 2 was water.

The distribution of grain sizes in the materials shown in Figure 12. Numerical values were assigned for the degree of roundness and sphericity of the sand grains by comparing the grain shapes with published charts (Krumbein and Sloss, 1951, p.81).Grains which approach a perfect sphere have the highest values of roundness and sphericity (maximum value equals 1.0).

	<i>Roundness</i>		<i>Sphericity</i>	
	<i>Range</i>	<i>Average</i>	<i>Range</i>	<i>Average</i>
Material 1 and 2	0.1-0.9	0.45	0.3-0.9	0.65
Material 3	0.8-1.0	0.90	0.8-1.0	0.90
Material 4	0.1-9.0	0.65	0.3-0.9	0.70

Measurements of the strength of the modeling materials were made in two ways. In the first, the fracture characteristics for the material, τ_0 and ϕ , were determined by placing the material in a rectangular container and removing the support for one vertical edge. The angle of fracture caused by removal of support at one vertical edge is related to the angle of internal friction by

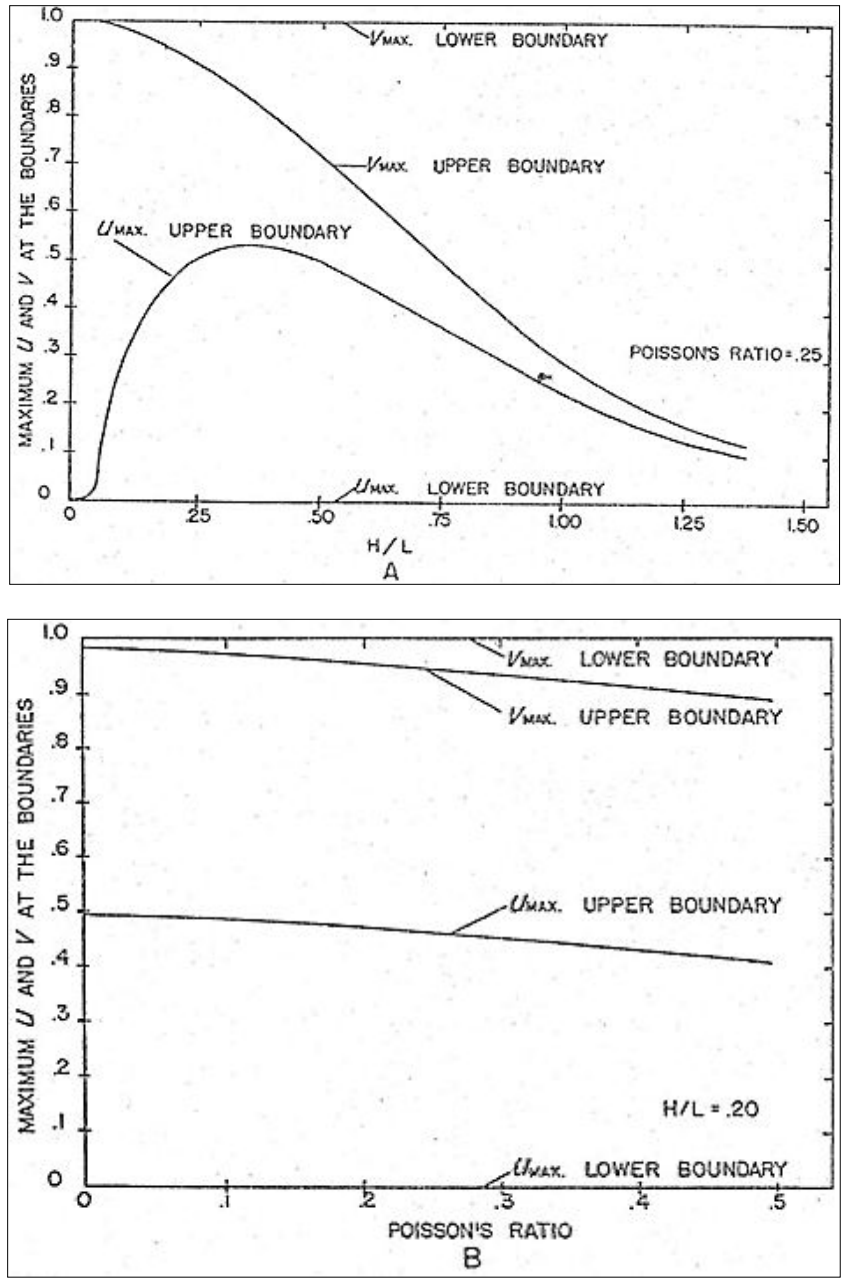


Figure 7 . Category I: Effect of Layer Dimensions and Poisson's Ratio on Displacements at Layer Boundaries. A show relative change in maximum displacements at layer boundaries with change in layer dimensions; B show relative change due to change in value of Poisson's ration.

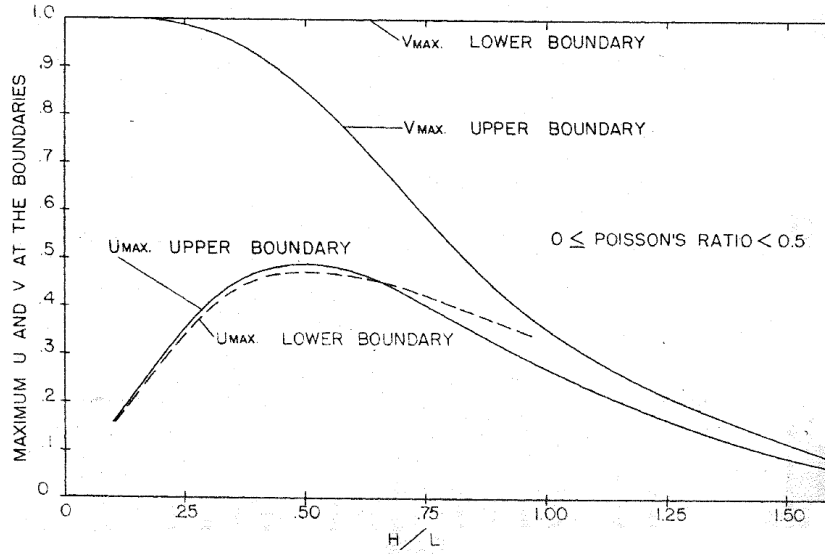


Figure 8 . Category III: Effect of Layer Dimensions on Displacements at Layer Boundaries.

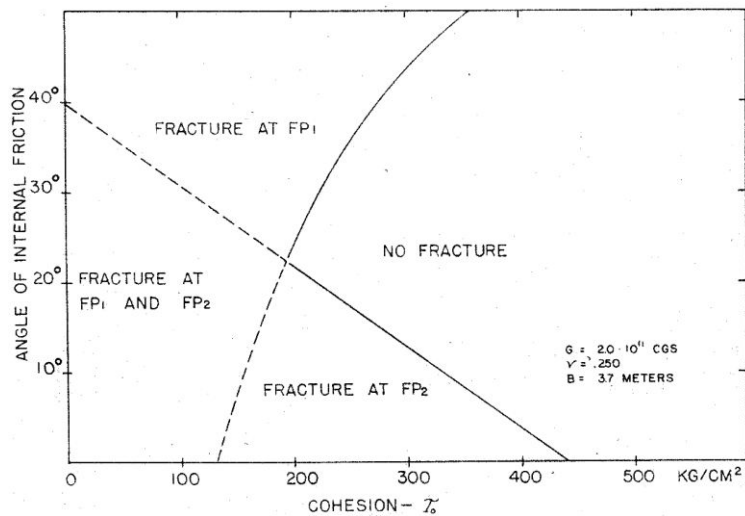


Figure 9. Example II a: Fracture Point Location as a Function of Layer Fracture Characteristics. Location of fracture point in example IIa (F_1 or F_2 on Figure 6B) is a function of fracture characteristics of the material of the layer.

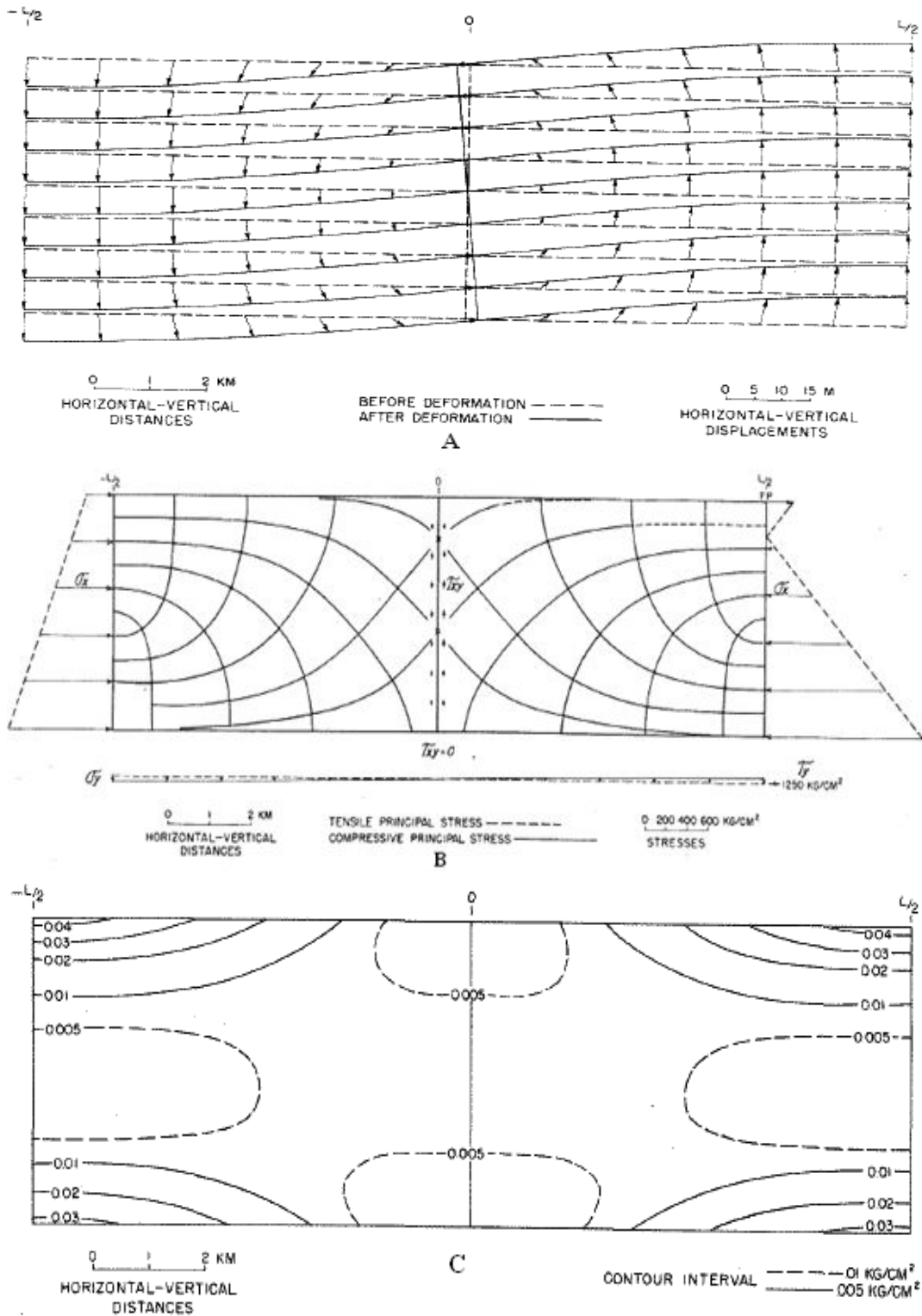


Figure 10 . Example IIIa, Diagrams: ,A—Displacement Field; B—Stress Distribution; C—Distortional Strain-Energy Density. In example IIIa, the lower boundary of an elastic layer 5 kilometer thick and 15.7 long undergoes half a wave length of sinusoidal vertical displacement and half a wave length of sinusoidal horizontal displacement (90° out of phase with the vertical).

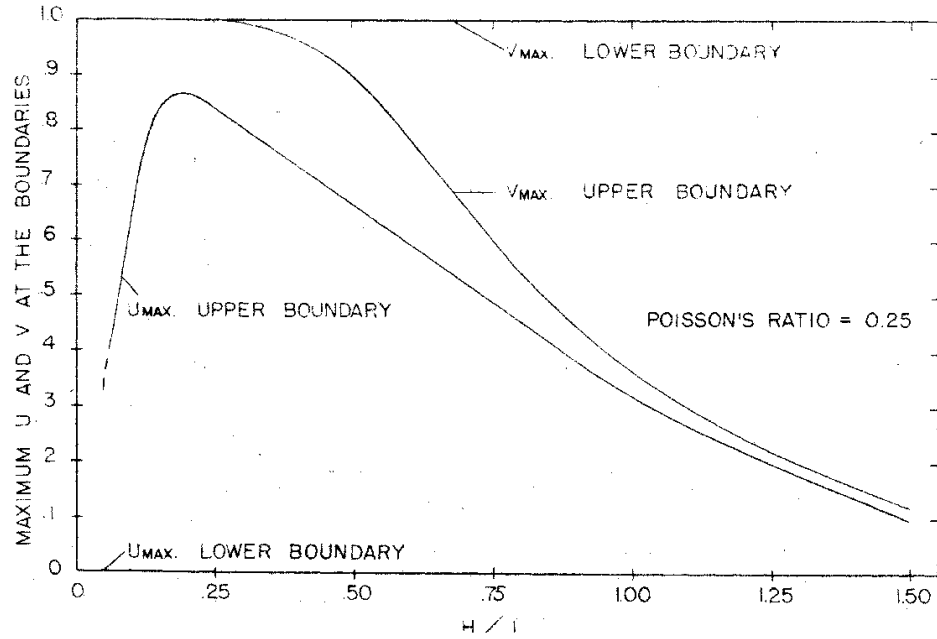


Figure 11 . Category III: Effect of Layer Dimensions on Displacements at Layer Boundaries. Figure shows relative change in maximum displacements at layer boundaries with change in layer dimensions .

$$\theta = 45^\circ - \frac{\phi}{2}, \quad (60)$$

If the material possesses cohesive strength, an unsupported vertical edge of a thin layer will stand without fracturing. The maximum thickness or critical height (h_{cr}) without fracture is related to the cohesive strength (Tschebotarioff, 1952 , p. 169 - 172):

$$\tau_0 = \frac{\rho g h_{cr}}{4 \tan \theta}, \quad (61)$$

(Equations (60) and (61) assume the special linear case of the Mohr fracture criterion.) Equation (61) does not consider the horizontal tensile stresses introduced by movement of material prior to fracture. These horizontal tensile stresses are located near the surface close to the unsupported edge. In as much as the tensile strength of granular materials is low, vertical tensile fractures form at the surface before shear fracture occurs lower in the layer. Formation of the tensile cracks reduces the critical height. The maximum depth of the cracks is estimated to be one-half the critical height (Tschebotarioff, 1952, p. 171). Thus, the maximum effect of the tensile cracks can be considered qualitatively by multiplying the observed critical height by 3/2.

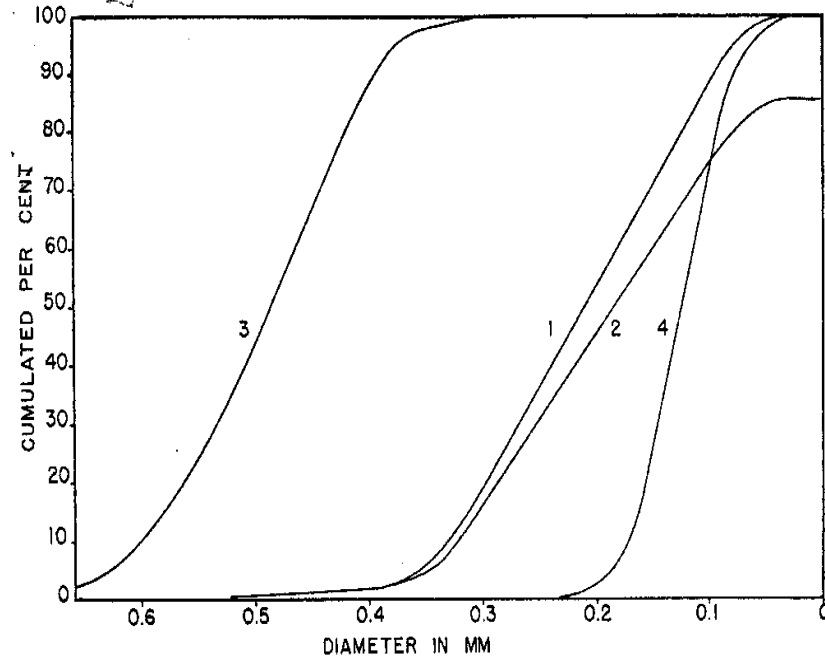


Figure 12 . Distribution of Grain Sizes in Modeling Materials

This method was applied to all modeling materials with the following results:

	<i>Uncompacted</i>		<i>Compacted</i>	
	τ_0 (dynes /cm ²)	ϕ	τ_0 (dynes/cm ²)	ϕ
Material 1	0	34°	0	54°
Material 2	140-210	42°	1100-1700	58°
Material 3	0	22°	0	45°
Material 4	0	27°	0	52°

The strength measurements were taken under conditions similar to those used in the experiments. In the uncompacted tests, material was poured into the box. In the compacted tests, material was placed in the box by layers which were moderately tamped (*approximately* > 10,000 dynes/cm²) after each layer was added.

The second procedure used for measurement of strength was the controlled-strain shear test (Tschebotarioff, 1952, p. 143-145). With these tests, the shear strength of Material 2 was determined under very low confining pressures. Tests were conducted for two degrees of compaction, strong and moderate (Figure 13). The material fractures according to the special linear case of the Mohr criterion. Although the data are scattered at low normal stresses, the best curves drawn by eye give the following values of τ_0 and ϕ for Material 2:

	<i>Strong Compaction</i>	<i>Moderate Compaction</i>
τ_0	4000 dynes/cm ²	1000 dynes/cm ²
ϕ	53°	40°

Also plotted on Figure 13 are data for controlled-strain shear tests on moderately compacted dry clay.

Model apparatus - The model experiments were performed in a rectangular box (inside dimensions 44.5 by 22.8 by 11.4 cm) with glass sides and wooden ends (PL 1). The bottom of the box was fitted with three felt-edged blocks for experiments that required steps in vertical displacement at the base of a layer. Each block could be moved independently in the vertical direction by four screws projecting through the bottom of the box.

The bottom of the box was fitted with a felt-edged rubber pad for experiments that required gradual changes in vertical displacement at the base of a layer. The central and end portions of the rubber pad could be moved independently in the vertical direction by screws projecting through the bottom of the box.

At the two ends of the box were vertical blocks, which followed the vertical movement of the end blocks or end portions of the rubber pad. This feature eliminated the drag which would occur if the ends of the box were fixed.

One feature of the apparatus may influence the experimental result the drag of the material along the glass face. Theoretically this drag should be zero if the model is to represent accurately the deformation normal to the long axis geologic structure. Controlled-strain shear tests were performed to find the coefficient of friction between Material 2 and a glass surface (Figure 13). The normal stress of Material 2 against the glass face in the box angled from 0 to 10,000 *dynes/cm*². The maximum coefficient of friction for this range of normal stress is 0.12. This agrees closely with the coefficient of friction for quartz grains moving over a solid quartz plate (Tscheboarioff, 1952 , P. 122-124). Inasmuch as the measured coefficient for Material 2 moving layer a glass surface was only one-fifth to one twenty-fifth the coefficient of friction of Material 2 over Material 2, drag along the glass face probably did not have a major influence on the experimental results.

Experimental procedure - Material was placed in the box in successive layers 0.6 – 1.2 *cm* thick. These layers were separated by thin marker lines of flour or quartz sand dyed black. It extended a short distance into the box from the glass face. Two degrees of compaction were used after each layer was added—zero and approximately 10,000 *dynes/cm*².

Displacements were applied to the base of the layer in small increments. Direct and oblique photographs (PI.1) of the model were taken between intervals of displacement. In some instances, several increments of displacement were recorded in a multiple exposure (Pi. 2). This was used to record displacement fields. The total time required for a complete experiment was about 1 hour.

Results of experiments

General statement - Two types of experiments were performed in the model studies. In Type I, a broad curve in vertical displacement was applied to the lower boundary of a homogeneous layer. In Type II, a step in vertical displacement was applied to the lower boundary of a homogeneous layer. Layers of each kind of modeling material were used one or more times in both types of experiments. The experiments performed were:

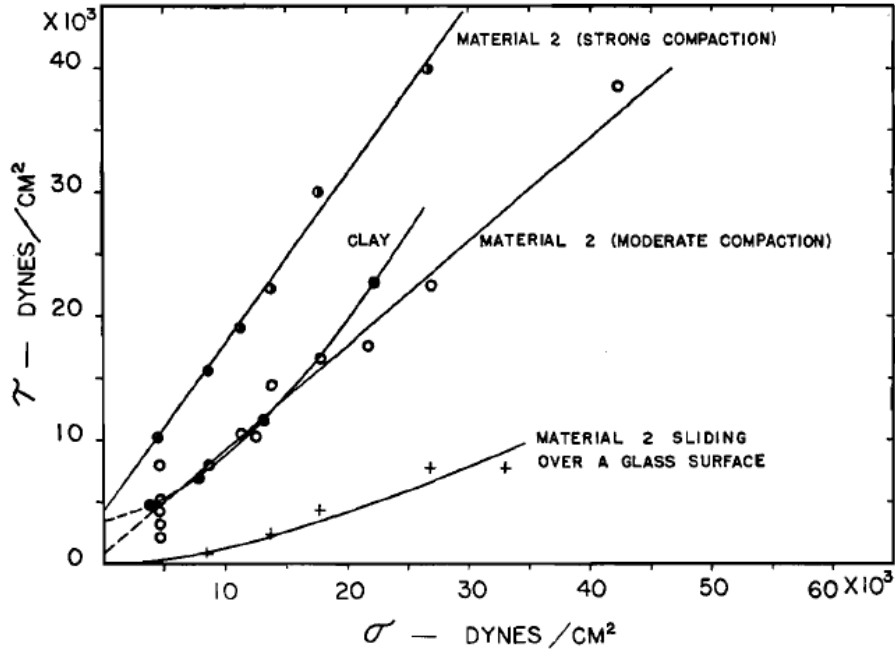


Figure 13. Results of Controlled-Strain Shear Tests

	Experiments With Material				Total Experiments
	1	2	3	4	
Type I	1	2	3	1	7
Type II	2	13	3	1	19

Several figures showing different stages of deformation in the model experiments have been used in the discussion of experimental results. These figures are tracings of photo graphs taken during the experiments. The coordinates for the figures are the same as those used in the numerical examples (see Figure 1).

Type i displacement fields - Figure 14 gives examples of the observed displacement fields. The important features of the displacement fields were:

1. No measurable change in the displacement field with a change in the composition of the layer.
2. An increase in horizontal displacement from the lower to the upper boundary of the layer.
3. Maximum horizontal displacement at or very near the point of inflection in the fold ($x = L/2$ or $-L/2$).
4. A decrease in vertical displacement from the lower to the upper boundary of the layer.

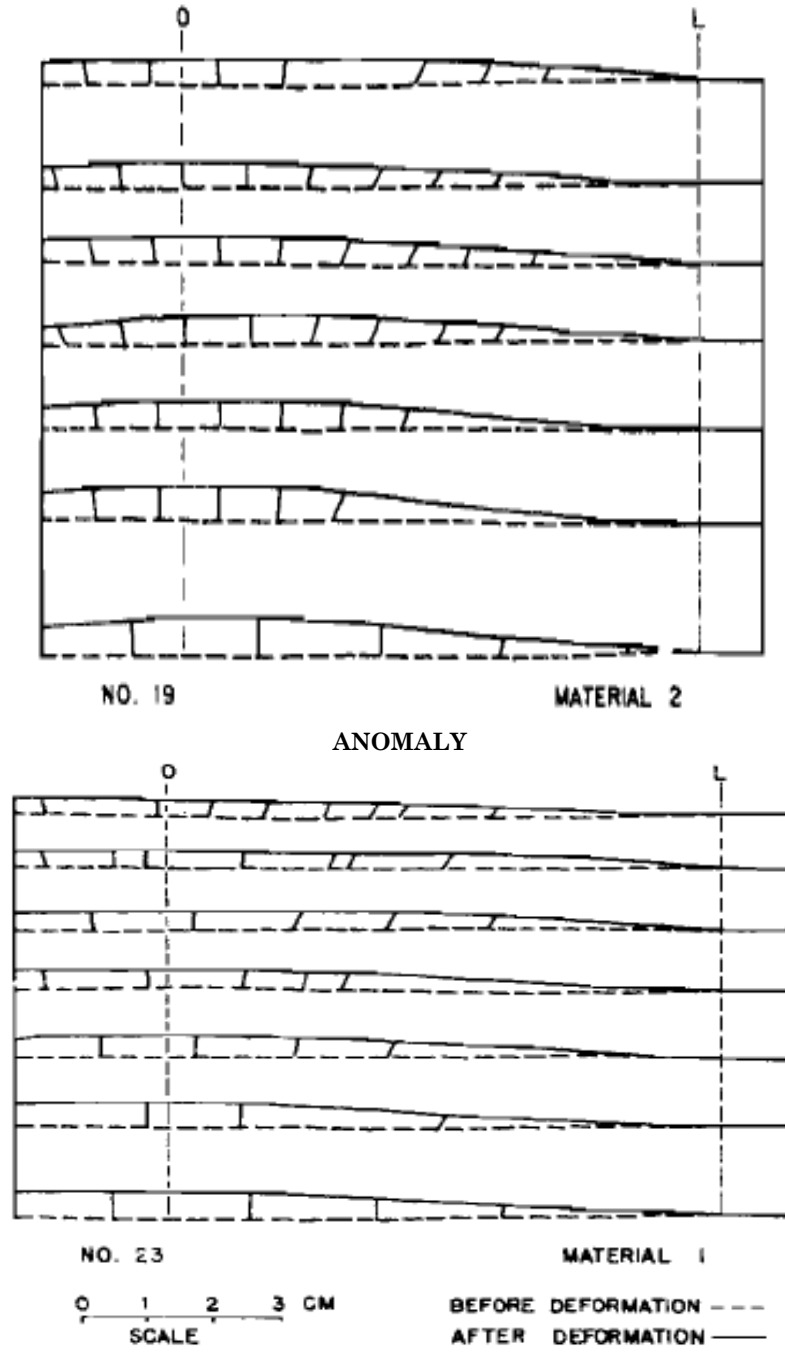


Figure 14. Displacement Fields - Type I Experiments

Type i fractures with material 2 - only models in which layers of Material 2 were used produced fracturing at large displacements (See No. 9 and No. 19 of Figure 15). The sequence of fracture formation with increase in applied displacement was as follows:

1. Vertical tensile cracks at the crest of the fold.
2. A series of normal faults at or near the crest of the fold.
3. Additional normal faults intersecting the surface at progressively greater distances from the crest of the fold.

The depth of the tensile cracks was not greater than 1 cm and in most cases was much less. The major normal faults were straight, had maximum displacement at the surface, and clipped toward the axis of the fold. Average dip of the major normal faults was 65° .

The angle of fracture and the depth of the tensile cracks (equivalent to the unsupported height in the strength measurements) can be used to determine the strength of the material in the layer at the time of fracture. The computed angle of internal friction from equation (60) is 40° . The computed cohesive strength from equation (61) is 100—200 *dynes/cm²*. These values are nearly identical to the values found in the strength measurements of un-compacted samples of Material 2.

Type i deformation with materials 1, 3 and 4 - No fracturing was observed in the experiments with layers of Materials 1, 3, and 4. However, a cup-shaped area over the crest of the fold was disturbed by the folding (No. 23 and No. 21 in Figure 15). The main features of the disturbed zone were blurring of the marker lines, flattening of the upper boundary, and thinning of the layer. The thinning over the crest of the fold was about 6 per cent of the original thickness for an applied vertical displacement of **1 cm** at $x = 0, y = H$.

Type ii displacement fields - Figure 16 gives examples of the observed displacement fields. The important features of the displacement fields were:

- (1) No measurable change in the displacement field with a change in the composition of the layer.
- (2) An increase in horizontal displacement from the lower to the upper boundary of the layer.
- (3) Maximum horizontal displacement at or very near $x = L/2$ or $-L/2$ along any horizontal line through the layer.
- (4) A progressively less abrupt transition in vertical displacement from the lower to the upper boundary of the layer.

Type ii fracture with material 2 - Type II experiments with layers of Material 2 produced distinct fractures at large applied vertical displacements (Figure 17). The usual sequence of fracture formation with increasing applied typical displacement was:

1. Simultaneous or nearly simultaneous formation of tensile cracks at the upper boundary and shear fractures at the lower boundary.
2. Propagation of one or more shear fractures (reverse faults) to the surface and deepening and widening of the tensile cracks (Figure 17).
3. Formation of normal faults in the tensile crack zone (No. 12 of Figure 18).
4. Formation of a major normal fault from the tensile crack zone to the edge of the uplifted block at the lower boundary of layer (No. 12 of Figure 18).
5. In most of the experiments, a series of reverse faults rather than a single fault formed at the edge of the uplifted block. Formation of these fractures followed a definite sequence; progressively younger fractures started at progressively smaller angles to the vertical edge of the uplifted block. The end result was a series of diverging fractures, the oldest starting at about 8° to the vertical, and the youngest starting vertically. Most of the fractures that started at an angle to the vertical propagated only a short distance. Many of these fractures were probably undetected in the experiments. Most of the fractures that started vertically eventually extended

all the way to the upper surface. The applied vertical displacement that was required to propagate a shear fracture all the way to the upper surface was equal to about one-twentieth of the total length of the fracture. The same ratio between applied displacement and length of fracture (1 to 20) appeared to hold for all intermediate stages in the development of the fracture as well.

6. The most interesting feature of the reverse faults (Figures 17 and 18) was the curvature of the line of fracture away from the uplifted block. Two factors influenced the curvature of the reverse faults, (1) the thickness of the layer, and (2) the number of short reverse faults formed before a particular reverse fault propagated to the surface. The influence of the second factor on curvature was eliminated by omitting the vertical portion of the fractures in the curvature measurements. These measurements were then correlated with an effective thickness (H') for each layer which was equal to the vertical distance over which the fracture actually curved (Figure 17).
7. Curvature measurements for three intervals of effective thickness are summarized in Figure 19. Although curvature measurements in adjacent intervals of effective thickness overlap, the mean values in each interval show a small systematic change of curvature with the effective thickness of the layer. With a decrease in the effective thickness, the fractures have (1) progressively greater curvature and (2) progressively lower dip at the upper surface.

The curvature of the reverse faults was independent of the relative movement of the blocks. In one experiment, the center section was allowed to drop while the two end sections remained stationary. The reverse faults produced by this mode of displacement were nearly the same as the reverse faults produced by keeping the center section stationary and pushing the two end sections (Nos. 3, 4, 5 and 8 of Figure 17).

In all Type II experiments with Material 2, displacements occurred along the reverse faults after they had reached the upper surface. As a result of this movement, thin wedges of material were thrust out over the upper surface of the stationary blocks. In one experiment (Figure 2 of Pl. 2), the horizontal movement of the front of the wedge was 0.5 *cm* after a total of 2.0 *cm* vertical displacement of the lower boundary.

In most of the experiments, vertical tensile cracks appeared at the upper surface at nearly the same time as the reverse faults were formed. The measured positions of the tensile cracks for three intervals of effective thickness are summarized in Figure 19. There is a systematic shift of the crack position with a change in the effective thickness of the layer.

Fracturing in the region of the tensile cracks followed the same pattern as the fracturing at the crest of the folds in the Type I experiments. The tensile cracks became deeper and wider with increased applied displacement. Eventually the crack reached a critical depth at which the material on each side of the crack was unable to support itself, and normal fractures dipping toward the tension zone were formed. The maximum depth of the tensile cracks before normal faults were formed was 2.5 *cm*.

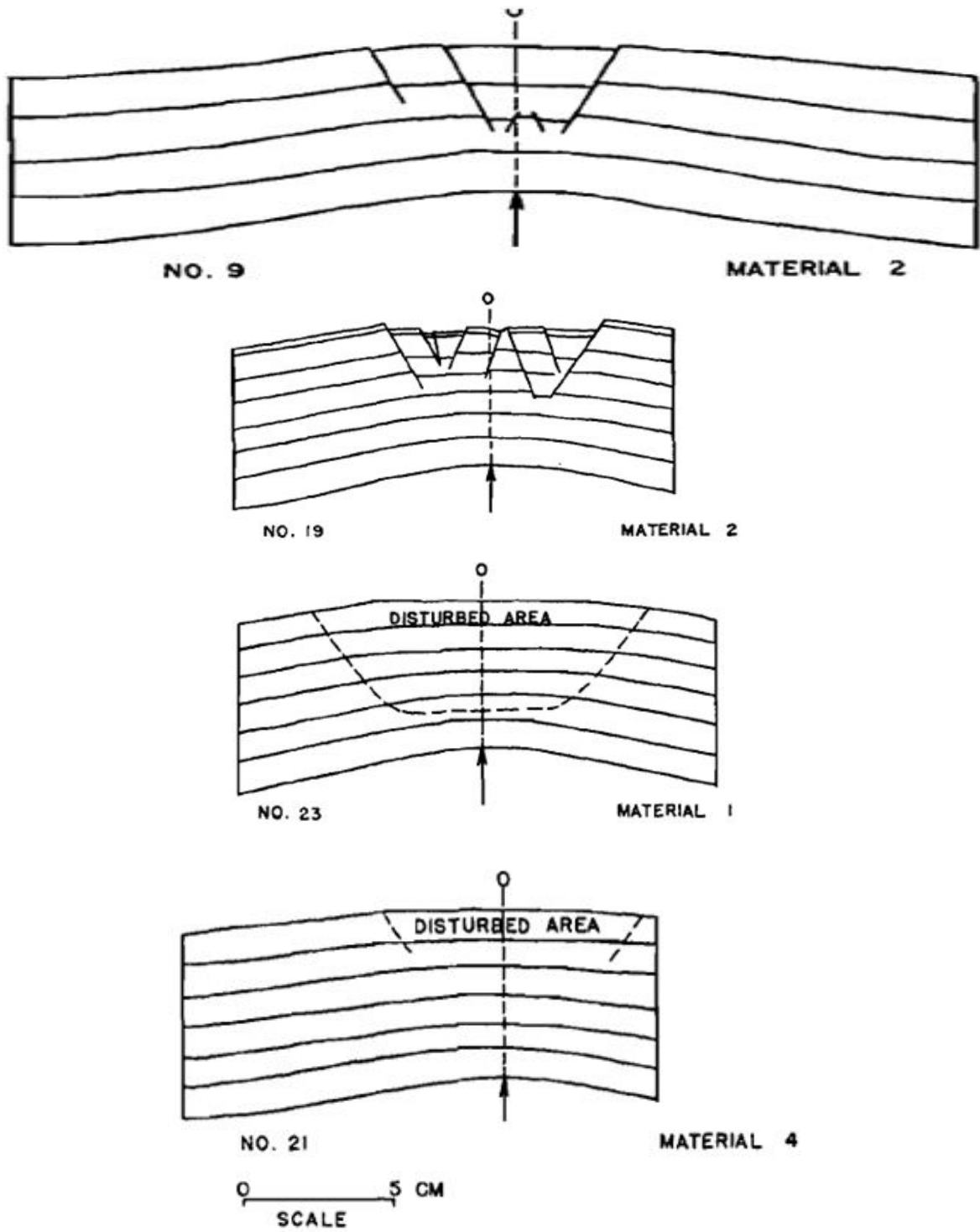


Figure 15 . Fracturing and Folding -Type I Experiments.

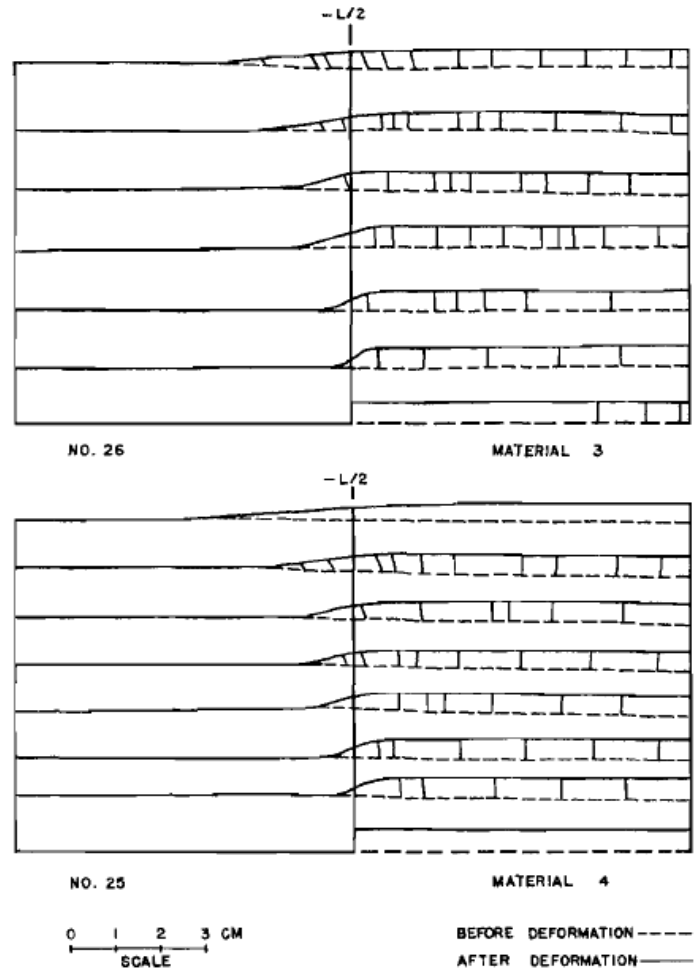


Figure 16 . Displacement Fields - Type II Experiments.

The final fracturing in the experiments was the propagation of a steep normal fault (average dip 78°) from the tensile crack zone to the edge of the uplifted block. After formation of the normal fault, displacement occurred along both the normal fault and the reverse faults. However, more displacement occurred along the normal fault than along the reverse faults.

The depth of the tensile cracks and the angle at which the reverse faults intersected the upper surface can be used to estimate the strength of the material in the layer at the time of fracture. The computed cohesive strength from the depths of the tensile cracks is $200 - 500 \text{ dynes/cm}^2$. The angle of internal friction from the average angle at which the fractures intersected the free upper surface (29°) is 32° . These values are fairly close to those obtained in the strength measurements on uncompacted samples of Material 2.

Type ii fractures with materials 1 and 4 - The fracture behavior of layers of Materials 1 AND 4 differed in two respects from the fracture behavior of layers of Material 2; (1) tensile cracks were not formed (No. 8 of Figure 17); and (2) the reverse faults formed were not sharp breaks, but narrow shear zones (No. 25 of Figure (18)). The curvature of the shear zones, however, was nearly identical with the curvature of the sharp reverse faults produced in the experiments with layers of Material 2.1 ayers of Material 1, which has a greater range in grain sizes and more

irregularity in grain shape and roundness than Material 4, had narrower zones of fracture than layers of Material 4.

Type ii deformation with material 3 - Folding rather than fracturing was dominant in experiments in which layers of Material 3 were 4ised. However, there were broad zones in the layers where the movement of the sand particles described trajectories which curved away from the uplifted block. In addition, ridges were formed on the upper surface similar to those associated with the reverse faults in the other experiments.

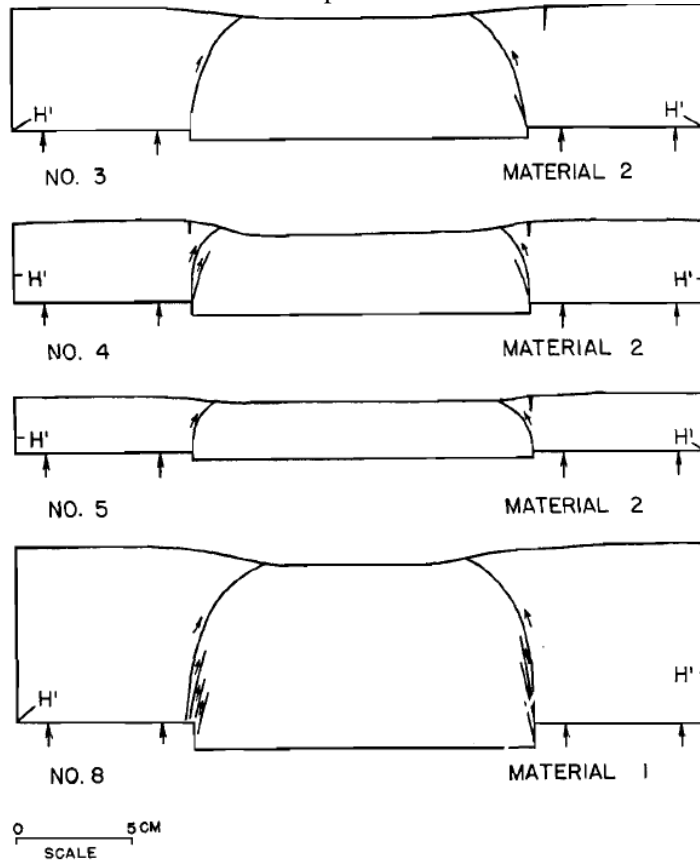


Figure 17 . Fractures - Type II Experiments

Summary of experimental results - The displacement fields, at small applied vertical displacements, appeared to be independent of the size, shape, and sorting of the grains used for the layers. Fracture, however, was influenced by the properties of the modeling materials. The sharpest fractures were formed in layers of material which had cohesive strength (Material 2). The next sharpest fractures were formed in layers of material which lacked cohesive strength but were composed of poorly sorted, irregular sand grains (Material 1). Layers composed of well-sorted, well-rounded, and spherical sand grains (Material 3) did not appear to fracture.

The strength of the material in the layer at the time of fracture was nearly the same as measured strengths of compacted samples of the modeling materials. Movement of the layer prior to fracturing apparently decreased the initial compaction of the material and thus reduced its strength.

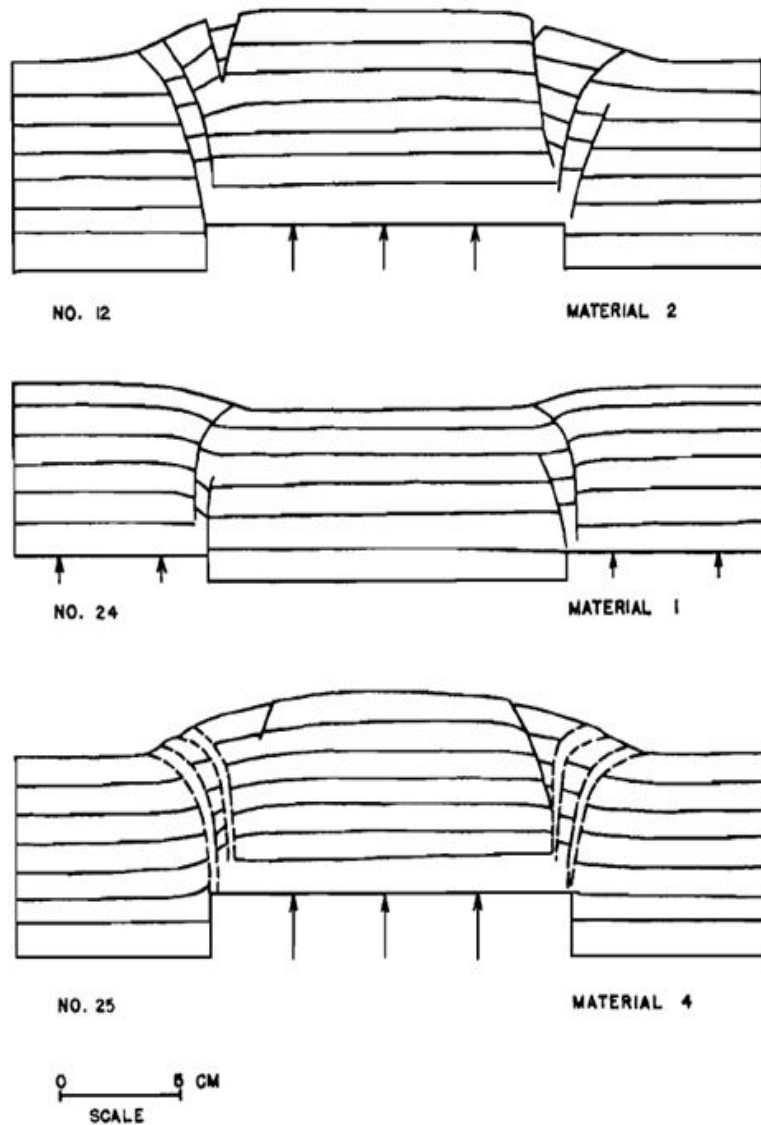
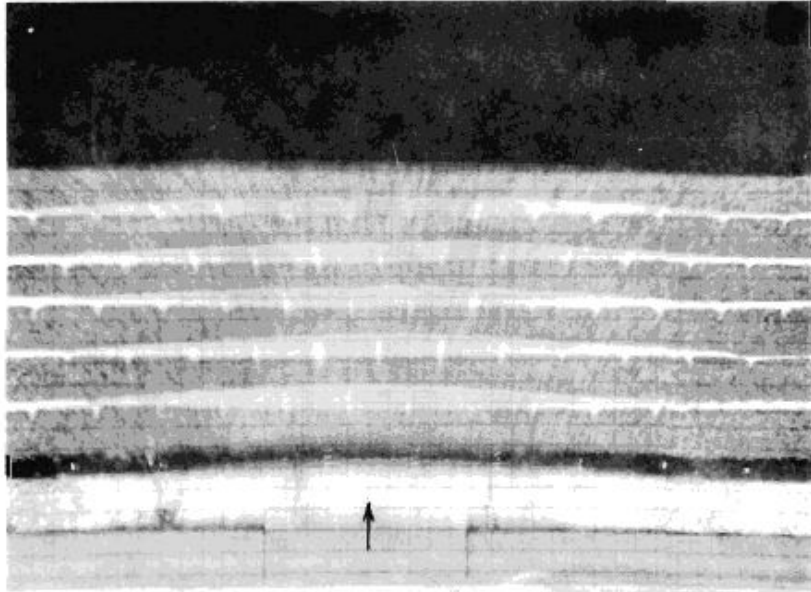


Figure 18 . Fracturing and Folding - Type II Experiments

Geologic interpretation of experimental results

Size relationship between model and geologic structure - The size relationship between a model and the geologic structure that it represents is determined from equation (59). The model ratios of strength and density must be known to use this equation. Unfortunately, there is no means of estimating the strength of extensive layers of sedimentary rock in nature. The strength is probably determined to a large extent by the degree of jointing in the layer. Layers of rock which have undergone extensive jointing have little or no cohesive strength and probably react to applied vertical displacements like layers of Material 1 do in the model experiments. Layers of rock, which have not undergone jointing, have a cohesive strength and probably react to applied vertical displacements like layers of Material 2 do in the experiments.

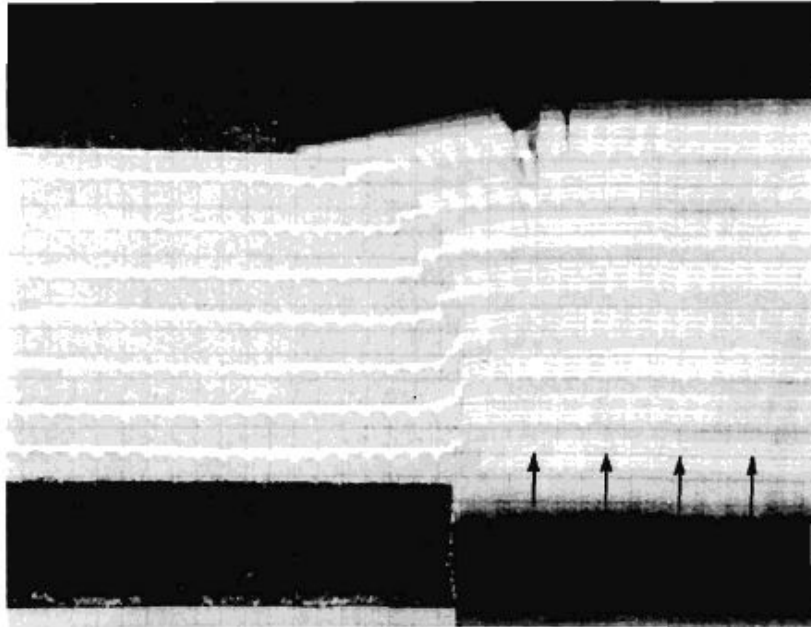


No. 23

Material 1

(GRID LINES ARE 0.5 CM APART)

FIGURE 1. — TYPE I EXPERIMENT — MULTIPLE EXPOSURE

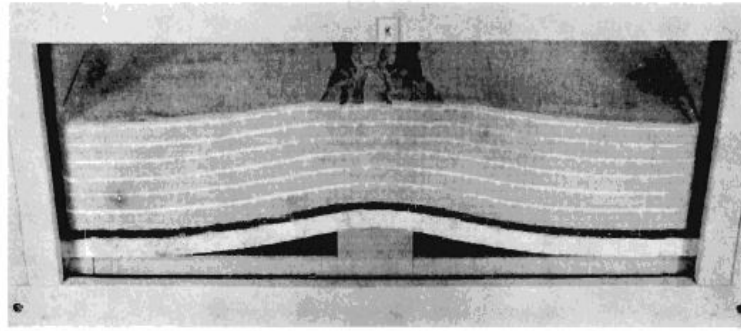


No. 15

Material 2

(GRID LINES ARE 0.5 CM APART)

FIGURE 2. — TYPE II EXPERIMENT — MULTIPLE EXPOSURE

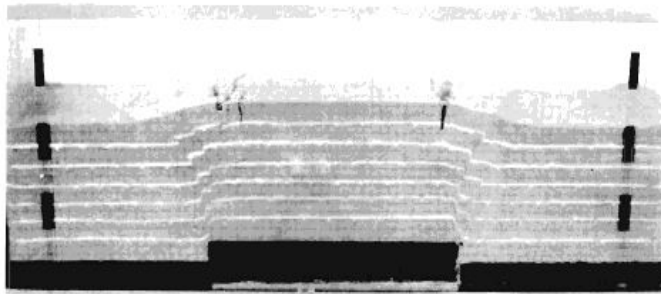


No. 19

Material 2

(GRID LINES ARE 0.5 CM APART)

FIGURE 1. — TYPE I EXPERIMENT



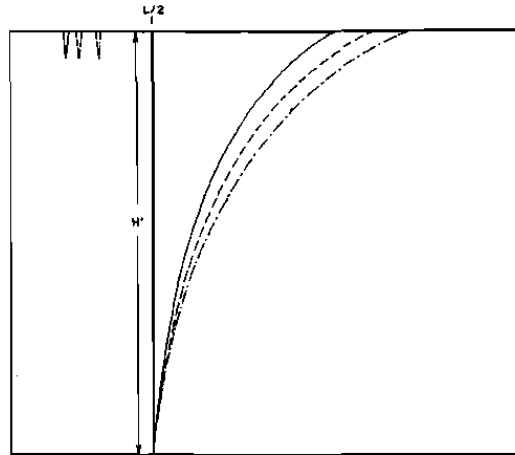
No. 12

Material 2

(GRID LINES ARE 0.5 CM APART)

FIGURE 2. — TYPE II EXPERIMENT

OBLIQUE PHOTOGRAPHS
OF EXPERIMENTS



$7.5 < H' \leq 100 \text{ CM}$ ———
 $5.0 < H' \leq 7.5 \text{ CM}$ - - -
 $2.5 < H' \leq 5.0 \text{ CM}$ - - -

Figure 19 . Curvature of Reverse Faults in Type II Experiments. Reverse faults in Type II experiments had (1) progressively greater curvature and (2) progressively lower dip at the upper surface with a decrease in the effective thickness of the layer.

A rock layer with no cohesive strength can be modeled with dry sand (similar to Material 1) which also has no cohesive strength. If the angles of internal friction in the sand and the rock layer are equal, the strengths of the layers are identical. However, the cohesive strength of the rock layer is zero only if one considers an extensive layer. The individual pieces between joints have considerable cohesive strength. The strength of the sand and rock layers will be identical only when the dimensions of individual blocks are related to the size of the rock layer in somewhat the same manner as the individual grains are related to the size of the sand layer.

Equation (59) cannot be used to establish a size relationship between the model and the geologic structure if the rock and the sand layers have no cohesive strength. However, a crude size relationship can be obtained by comparing the size of sand grains with the size of joint blocks. The mean grain diameter for Material 1 is 0.2 mm . A reasonable diameter for a joint block is 10 m . The size relationship based on the above values is 1 cm of Material 1 equals 0.5 km of jointed rock.

A relationship between the size of the model and the geologic structure can be established with equation (59) if the layer of rock in the geologic structure has a cohesive strength. A rock layer with cohesive strength can be modeled with Material 2 which has a small cohesive strength of 1000 dynes/cm^2 and an angle of internal friction of about 40° . Representative values of cohesive strength and angle of internal friction for sedimentary rock are $250 \times 10^6\text{ dynes/cm}^2$ and 40° . The size relationship, on the basis of the above values, is 1 cm of Material 2 equals 1.5 km of sedimentary rock.

The τ_0 and ϕ values used to establish this size relationship are based on controlled-strain shear tests of moderately compacted samples of Material 2 and triaxial tests on small samples of sedimentary rock. In the model experiments, the strength of a moderately compacted layer of Material 2 is considerably reduced by deformation of the layer prior to fracturing. A similar reduction in the strength of a layer of sedimentary rock probably occurs in nature. However, the strengths of the two layers may not be reduced in the same proportion. For this reason, the size relationship between the model and the geologic structure may change during the course of an experiment.

Fractures - The characteristic fracture pattern for Type I experiments is a complex zone of normal faults at the crest of the fold (Figure 15). The fractured zone tapers inward to the axis of the fold and dies out at depth. The Kettleman Hills anticline (Woodring et al., 1940) has this type of fracture pattern.

The characteristic fracture pattern for Type II experiments is a series of curved reverse faults intersecting the upper surface at low angles, and a series of normal faults in the uplifted block (Figure 18). The reverse faults start as vertical faults at the lower boundary but become thrusts at the upper boundary. The low-angle or thrust portion of the fracture at the upper surface is due to horizontal compressive stresses. However, the horizontal compression is the result of vertical movement at depth and not of horizontal compression of the entire layer.

The characteristic fracture pattern formed for each of the two types of experiments is perhaps the most significant feature of the model experiments. Each pattern is relatively complex in view of the simplicity of the two distributions of applied displacement. The individual fractures in each pattern are related. Formation of one fracture triggers another in a definite sequence. The type and location of the primary fractures, which initiate the fracture sequence, are controlled by the distribution of applied displacement. The type and location of secondary

fractures are determined partly by the distribution of applied displacement and partly by conditions arising from the formation of the primary fractures.

The manner in which the fracture pattern forms in the two types of experiments suggests that other distributions of applied displacement the base of a layer may also lead to distinctive fracture patterns. If the models are a true representation of fracturing in nature, fracture patterns observed in the models might be compared with fracture patterns observed fracture the surface of the earth, and in this manner be used to determine the distribution of displacement at depth.

Comparison of experimental and analytical results Type i experiments and category i numerical examples

Displacement fields - The displacement fields in Type I experiments and Category I numerical examples are very similar, although this is not immediately apparent from an examination of the displacement-field diagrams. Displacement fields in the analytical work (Figures 4 A and 5 A) are produced by applied vertical displacements which change periodically in amplitude and direction. Displacement fields in the experimental work (Figure 14) are produced by applied vertical displacements which change amplitude but not direction. The only major difference between the two displacement fields as a uniform displacement in one direction. As previously noted, uniform movement of a layer does not change the stress distribution. Therefore, superposition of a uniform upward displacement (equal to one-half the total amplitude of the applied vertical displacement) on the analytical displacement field will bring the two displacement fields into approximate agreement.

Although the general appearance of the displacement fields is similar, they differ considerably in detail. The maximum vertical and horizontal displacements at the boundaries of the model and the corresponding theoretical displacements from Figure 7 A (for the average H/L ratio of 0 – 85 in the experiments) are

	<i>Experimental</i>	<i>Theoretical</i>
v_{max} . Lower boundary	$1.00B$	$1.00B$
v_{max} . Upper boundary	$0.60B$	$0.40B$
u_{max} . Lower boundary	$0.30B$	$0 B$
u_{max} . Upper boundary	$0.70B$	$0.30B$

(B equals the maximum applied vertical displacement)

Two factors are responsible for most of the difference between theoretical and experimental value above .First, the boundary conditions in the experiments differed slightly from the boundary conditions in the analytical examples. In the experiments, the applied vertical displacement did not vary exactly as the cosine of the horizontal distance, and horizontal displacement occurred along the lower boundary. Second, the displacements required in the experiments to record the displacement fields photographically were much larger than the critical displacements (B_c) in the analytical work. In nearly all the experiments, there was evidence of failure in the layer while the displacement field was being photographed.

Fractures - In the experiments with layers of Material2, the position of the vertical tensile cracks is the same as the position of the initial tensile fractures predicted in the numerical examples.

Type ii experiments and category ii numerical example

Displacement fields - The general appearance of the displacement fields in Type II experiments (Figure 16) and Category II example (Figure 6.4) is very similar if a uniform upward displacement (equal to one-half the total amplitude of the applied displacement) is superposed on the analytical displacement field. However, the displacement fields differ slightly in detail. Listed below are the maximum vertical and horizontal displacements at the boundaries of the model and the corresponding theoretical displacements from Figure 8

(for the average H/L ratio of 0.47 in the experiments):

	<i>Experimental</i>	<i>Theoretical</i>
v_{max} .Lower boundary	$1.00B$	$1.00B$
v_{max} .Upper boundary	$0.95B$	$0.89B$
u_{max} .Lower boundary	$0B$	$0 B$
u_{max} .Upper boundary	$0.60B$	$0.67B$

(B Equals the maximum applied vertical displacement)

The difference between the experimental and theoretical values is small. In this case, the boundary conditions in the experimental work were nearly equivalent to the boundary conditions in the theoretical example. Fracturing in the layer while the displacement fields were being photographed probably accounts for most of the difference in the experimental and theoretical values.

Fractures - The predicted positions of the reverse faults in the Category II numerical example are based on the stress distribution in Figure 6B and equation (50). The constant angle obtained from equation (50) is the orientation of the reverse faults with respect to the position of maximum compressive principal stresses throughout the layer. In as much as the principal stress trajectories are curved, the reverse faults will also be curved. In Figure 20, three reverse faults based on the stress distribution have been drawn for three different angles of internal friction. Also shown on Figure 20 is a shear fracture based on measurements of reverse faults in model experiments which were geometrically similar to the numerical examples. The agreement between the experimental fracture and the theoretical fracture for a ϕ equal to 28° is very good. A value of 28° is a reasonable average angle of internal friction for the entire layer.

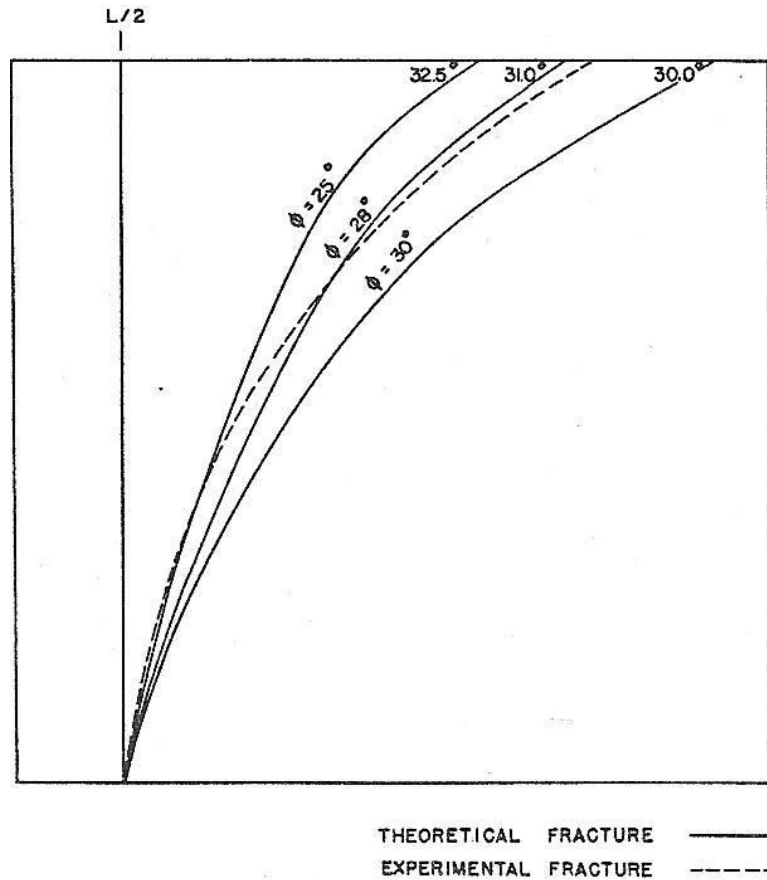


Figure 20. Comparisons of Theoretical and Experimental Fractures. The shear fracture determined from Example Ia stress distribution (Figure 6 B) and Molar's fracture criterion (with $\phi = 28^\circ$) agrees closely with the shear fracture in the experiments which were geometrically similar to Example Ia.

The tensile cracks in the experiments do not occur at the positions predicted in the analytical work (compare the position of tensile cracks on Figure 19 with the position of F_1 on Figure 6B). Apparently the formation of the reverse faults shifts the position of the large horizontal tensile stresses closer to the position of the reverse faults.

References

- Allen C. R., Amand P. ST. Richter C. F, and J. M. Nordquist , (1965) Relationship between seismicity and geologic structure in the Southern California region Bulletin of the Seismological Society of America,; 55(4): 753
- Brewer J. A., Cook F. A., Brown L. D., Oliver J. E., Kaufman S., and Albaugh D. S. (1981) COCORP seismic reflection profiling across thrust faults Geological Society, London, Special Publications,; 9(1): 501 - 511.
- Birch, F., (1942), Handbook of physical constants: Geol. Soc. America Special Paper 36, 325 p.
- Birch, F., (1951), Mechanical basis for certain familiar geologic structures: Geol. Soc. America Bull., v. 62. 355-372
- Couples G. D. and Lewis H. (1999) Effects of interlayer slip in model forced folds Geological Society, London, Special Publications,; 169(1): 129 - 144.
- Couples, H. G. D. Lewis, P. Olden, G. H. Workman, and N. G. (2007) Higgs Insights into the faulting process from numerical simulations of rock-layer bending Geological Society, London, Special Publications, 289(1): 161 - 186.
- Davies R. K. and Fletcher R. C. Shear (1990) bands in a plastic layer at yield under combined \ shortening

- and shear: a model for the fault array in a duplex Geological Society, London, Special Publications, ; 54(1): 123 –
- Faller A. M. ,and Soper N. J. (1979) Palaeomagnetic evidence for the origin of the coastal flexure and dyke swarm in central E Greenland Journal of the Geological Society,; 136(6): 737 - 744.
- Ferrill D. A., Morris A. P., and Smart K. J (2007) Stratigraphic control on extensional fault propagation folding: Big Brushy Canyon monocline, Sierra Del Carmen, Texas Geological Society, London, Special Publications, ; 292(1): 203 - 217.
- Gudmundsson A. and Nilsen K. (2006) Ring-faults in composite volcanoes: structures, models and stress fields associated with their formation Geological Society, London, Special Publications,; 269(1): 83 - 108.
- Gutenberg, B., (1951), Internal constitution of the earth: 2d ed., N. Y., Dover Publications, Inc., 438 p.
- Hafner, W., (1951), Stress distributions and faulting: Geol. Soc. America Bull., v. 62, p. 373-398.
- Hubbert, M. K., 193j, Theory of scale models as applied to the study of geologic structures: Geol...Soc. America.
- Jaeger, J. C., P956, Elasticity, fracture, and flow: N. Y., John Wiley and Sons, Inc.. 152 p.
- Krumbein, VV. C. and Sloss Stratigraphy and sedimentation: San Francisco, W. H. Freeman and Co., 497
- Murdoch J. N. , (1979) A tectonic interpretation of earthquake focal mechanisms and hypo centers in Ridge Basin, southern California Bulletin of the Seismological Society of America,; 69(2):
- Marti J., Ablay G. J., Redshaw L. T., and Sparks r. S. J. (1994) Experimental studies of collapse calderas Journal of the Geological Society,; 151(6): 919 - 929.
- McClay K.R., (1990) Deformation mechanics in analogue models of extensional fault systems Geological Society, London, Special Publications,; 54(1): 445 - 453.
- Marin, J., (1952), Engineering materials: N. Y., Prentice-Hall, Inc., 491 p.M. Barriere Deformation associated with the Ploumanac'h intrusive complex, Brittany Journal of the Geological Society, 1977; 134(3): 311 - 324.
- Murrell S. A. F. (1977) Natural faulting and the mechanics of brittle shear failure Journal of the Geological Society,; 133(3): 175 - 189.
- Mills, A. P., *et al.*, (1955), Materials of construction: 6th ed., N. Y, John Wiley and Sons, Inc., 130p.
- Muskhelishvili, N. I., (1953), Some basic problems of the mathematical theory of elasticity: 3d ed., Groningen- Holland, P. Noordhoff, Ltd., 04p.
- Langston C. A. The (1971) San Fernando earthquake: A study of source finiteness in teleseismic body waves Bulletin of the Seismological Society of America, February 1, 1978; 68(1): 1 - 29.
- Love, A. E. H.,(1944), A treatise on the mathematical theory of elasticity: 4th ed., N. Y.,Dover Publications, Inc., 643 .
- Phillips, H. B., (1933), Vector analysis: N. Y., John Wiley and Sons, Inc., 236 p. Timoshenko, S., and Goodier, J. N., 1951, Theory of elasticity: 2d ed.N. Y., McGraw-Hill Book Co., Inc.,506 p.
- Phipps C. B. and Reeve F. A. E Structural geology of the Malvern, Abberley and Ledbury hills Quarterly Journal of the Geological Society, 1969; 125(1-4): 1 - 37.
- Patton T. L. Sandbox models of downward-steepening normal faults AAPG Bulletin, , (2005); 89(6): 781 - 797. B. Kennedy, J. Stix, J. W. Vallance, Y. Lavallee, and M.-A.
- Longpre Controls on caldera structure: Results from analogue sandbox modeling Geological Society of America Bulletin, 2004; 116(5-6): 515 - 524.
- Sharp I. R., Gawthorpe R. L, Underhill J. R., and Gupta S. (2000) Fault-propagation folding in extensional settings: Examples of structural style and synrift sedimentary response from the Suez rift, Sinai, Egypt Geological Society of America Bulletin,; 112(12): 1877 - 1899.
- Tschebotarioff, G., (1952), Soil mechanics, foundations, and earth structures: 1st ed., N. Y., McGraw-Hill Book Co., Inc., 655 p.
- Vendeville B., (1991) Mechanisms generating normal fault curvature: a review illustrated by physical Models Geological Society, London, Special Publications; 56(1): 241 - 249.
- Yin H. ,and Groshong R. H. Jr. (2007) A three-dimensional kinematic model for the deformation above an active diapir AAPG Bulletin,; 91(3): 343 - 363.
- Woodring, W. P., Stewart, R., and Richards, R. W., (1940), Geology of the Kettleman Hills oil field, California: U. S. Geol.